Received 12 October 2023; revised 27 November 2023; accepted 3 December 2023. Date of publication 6 December 2023; date of current version 3 January 2024.

Digital Object Identifier 10.1109/OJCOMS.2023.3340091

Characterization of Orthogonal Chirp Division Multiplexing and Performance Evaluation at THz Frequencies in the Presence of Phase Noise

GIAMPAOLO CUOZZO [1] (Member, IEEE), NICOLÒ LONGHI [1,2] (Graduate Student Member, IEEE), AND GIANNI PASOLINI [1,2] (Member, IEEE)

[1]National Laboratory of Wireless Communications (WiLab), CNIT, 40133 Bologna, Italy
[2]Department of Electrical, Electronic, and Information Engineering, University of Bologna, 40136 Bologna, Italy

CORRESPONDING AUTHOR: G. CUOZZO (e-mail: giampaolo.cuozzo@wilab.cnit.it)

This work was supported in part by the European Union through the Italian National Recovery and Resilience Plan (NRRP) of NextGenerationEU, partnership on "Telecommunications of the Future" (Program "RESTART") under Grant PE00000001. The work of Nicolò Longhi was supported by Telecom Italia S.p.A.

ABSTRACT Due to its superior performance, Orthogonal Chirp Division Multiplexing (OCDM) has recently gained attention as a potential replacement for Orthogonal Frequency Division Multiplexing (OFDM) in beyond-5G systems. In this paper, we provide an analytical characterization of OCDM signals, elucidating the theoretical principles that enable their numerical generation through the Inverse Discrete Fresnel Transform (IDFnT), despite the presence of severe frequency-domain aliasing that substantially distorts the signal at the transmitter output. Furthermore, in light of the proposed utilization of the THz band in beyond-5G systems, we investigate the performance of OCDM in this frequency range in the presence of thermal, molecular, and phase noise. To model the latter, which is expected to be a significant challenge at THz frequencies, we take as a reference an actual Phase Locked Loop (PLL) oscillator operating at 237.7 GHz. The numerical results reveal the achievable performance of OCDM as a function of several key factors, including the modulation order, the bandwidth, the number of chirps constituting the signal, the oscillator parameters, the channel model, and the use of techniques aimed at mitigating the impact of phase noise. The findings are compared with those of OFDM, which is regarded as a benchmark due to its adoption in 4G and 5G systems, and demonstrate the superior performance of OCDM also in the presence of significant phase noise.

INDEX TERMS Orthogonal chirp division multiplexing, orthogonal frequency division multiplexing, phase noise, signal analysis, THz communications.

I. INTRODUCTION

MORE than 15 years ago, Orthogonal Frequency Division Multiplexing (OFDM) was selected as the waveform for 4G Long-Term Evolution (LTE) due to its high spectral efficiency, robustness in coping with severe channel conditions and its ability to easily multiplex data from multiple users on the same signal. Building upon the success of 4G, the 3rd Generation Partnership Project (3GPP) chose to adopt OFDM for 5G as well, enhancing it with advanced features to support Ultra-Reliable Low-Latency Communications (URLLC), Enhanced mobile Broad-Band (eMBB) communications, and massive Machine-Type Communications (mMTC). However, it is becoming increasingly clear that certain applications anticipated in the near future, such as intelligent vehicular mobility, extended reality, digital twins, and holograms, set up more stringent requirements that cannot be met even by 5G [1]. To meet the challenges posed by upcoming advanced applications, the use of new waveforms and the adoption of higher carrier frequencies, providing larger bandwidths, play a crucial role.

Concerning the adoption of new waveforms, Orthogonal Chirp Division Multiplexing (OCDM) [2], [3] has attracted attention recently as a particular extension of Affine Frequency Division Multiplexing (AFDM) [4]: similar to OFDM, which is based on the simultaneous modulation

and transmission of orthogonal carriers, OCDM performs the simultaneous modulation and transmission of orthogonal chirps, that is, of sinusoidal signals whose frequency varies over time, either in an upward or downward direction. Remarkably, by exploiting the intrinsic robustness to channel impairments of chirp signals, OCDM has been shown to provide better performance than OFDM, still achieving a spectral efficiency that approaches that of the Nyquist signaling [3] and offering the same Peak-to-Average Power Ratio (PAPR), as mathematically proven by [5]. More precisely, OCDM was proved

- to be more resilient than OFDM against inter-symbol interference due to insufficient guard interval [2];
- to perform better than OFDM in the presence of narrowband interference and time burst interference [5];
- to feature better Bit Error Rate (BER) vs Signal to Noise Ratio (SNR) performance than OFDM in multipath channels when linear or decision-feedback equalizers are adopted [2], [5].

Another significant advantage of OCDM over OFDM lies in its inherent compatibility with Pulse Compression (PC)-based channel estimation techniques. Specifically, since an OCDM signal consists of frequency chirps that span the signal bandwidth, this makes it possible to easily estimate the frequency response of the channel through the analysis of one or a few received chirps, which serve as pilot signals [6]. Moreover, basically for the same reasons, OCDM waveforms are also well-suited for radar-like applications. Indeed, the scientific literature is increasingly featuring articles that investigate the performance of OCDM systems used for both communication and sensing, comparing their performance with that of their OFDM-based counterparts [7], [8], [9] and showing that the former outperforms the latter when appropriate techniques are adopted [9].

Despite its superiority, OCDM is conceptually very similar to OFDM, the only difference being that the OCDM transmitter uses the Inverse Discrete Fresnel Transform (IDFnT) instead of the Inverse Discrete Fourier Transform (IDFT) to generate the samples of the (baseband) modulated signal. Remarkably, the Inverse Discrete Fresnel Transform (IDFnT) utilized by OCDM can be implemented based on the IDFT, thus enabling easy integration/coexistence with OFDM systems. This similarity also implies that the flexibility in resource allocation that is integral to OFDM's success also applies to OCDM. In both cases, users are assigned subsets of the available resource elements, namely subcarriers and time slots in the case of OFDM, and chirps and time slots for OCDM. It follows that, from the perspective of resource allocation flexibility, there is no significant difference between the first solution, which leads to Orthogonal Frequency Division Multiple Access (OFDMA), and the second solution, which leads to Orthogonal Chirp Division Multiple Access (OCDMA).

After reviewing the scientific literature, it is thus apparent that adopting OCDM, although entailing a slightly higher complexity due to the IDFnT implementation,[1] offers substantial advantages over OFDM, while still retaining the positive characteristics of the latter. It was this finding that sparked our interest in investigating the OCDM modulation, addressing still unexplored aspects. In this regard, Section II provides insights into the generation of OCDM signals through the discrete-time synthesis of its in-phase and quadrature baseband components, explaining how it results in signal distortion and why such distortion is actually beneficial. We point out that the results and insights presented in Section II are applicable to OCDM signals in general, regardless of the frequency band under consideration. They have been derived through a comprehensive analytical investigation, which constitutes the first original contribution of this paper.

The second part of the paper, specifically Sections III and IV, delves instead into the feasibility of OCDM as a prospective waveform candidate for 6G. In particular, this second original contribution concerns the evaluation of the performance of OCDM when operated in the THz frequency band, which is anticipated to be allocated for this technology [11], [12], [13], [14]. In this regard, excellent surveys addressing the prospective adoption of THz frequencies in future wireless communications can be found in [15], [16], [17].

Indeed, the development of transceivers operating at THz frequencies poses formidable challenges, such as the design of efficient power amplifiers as well as oscillators featuring low Phase Noise (PN). Specifically, the strong PN of high-frequency oscillators is a widely recognized critical factor that impacts the performance of sub-THz and THz systems: as is known, if a Phase Locked Loop (PLL) is employed in the carrier generation circuit, a P-times increase in the carrier frequency raises the PN effect by a factor $20\log_{10}(P)$ [18]. For instance, an increase in the carrier frequency from 1 GHz to 1 THz results in a 60 dB increase in the impact of PN, which makes it clear how important it is to consider this impairment when investigating THz communication links. In light of this, in the second part of this paper we provide a comprehensive investigation, carried by means of simulations, into the performance of OCDM in the presence of PN, which was modeled based on a real oscillator operating at 237.7 GHz, that is, in the THz band — typically defined as the [0.1 THz-10 THz] frequency range.

The remainder of this paper is organized as follows. In the next sub-section, we present a review of the literature mostly related to the content of this article and highlight the original contribution we provide. Section II investigates

1. It is well-known that the computational complexity of an IDFT consists in $\frac{N}{2}\log_2(N)$ complex multiplications and $N\log_2(N)$ complex additions per symbol time [10]. On the other hand, the IDFnT can be obtained from the IDFT with two additional phase rotations per symbol time, which leads to $\frac{3N}{2}\log_2(N)$ complex multiplications and the same number $N\log_2(N)$ of complex additions, as also underlined in [2]. Clearly, this additional computational effort of OCDM produces a higher energy consumption w.r.t OFDM that should be taken into account when opting for this multiplexing scheme.

the characteristics of numerically generated OCDM signals, revealing and analyzing the presence of aliasing in the frequency domain and providing the theoretical foundations that make the numerical synthesis possible despite the distortion it originates. Section III introduces the OCDM link we considered in our performance investigation, also providing the details of the adopted PN model, while Section IV compares the performance of OCDM and OFDM links at 237.7 GHz. Conclusions are drawn in Section V.

A. ORIGINAL CONTRIBUTIONS WITH RESPECT TO THE EXISTING LITERATURE

In 2016, Ouyang and Zhao introduced OCDM, showing that it performs better than OFDM [2], [3]. Later, this modulation technique was also considered for submarine links [19], [20], Multiple-Input Multiple-Output (MIMO) systems [21], [22], baseband powerline communications [23], powerline sensing [24], and uplink multiple access [25], [26]. Since OCDM is based on the use of chirp waveforms, some contributions also studied its adoption for radar applications [7], [24]. Several efforts have also been made to reduce the complexity of OCDM equalization procedures, like the ones proposed in [27], [28], [29], [30], [31].

Despite the large number of articles dedicated to this waveform, the literature lacks an analysis of OCDM that fully captures its characteristics. In fact, the signal is usually expressed using a matrix representation that, although very elegant, hides some of its characteristics. Contrarily, this paper provides a comprehensive analysis of OCDM, which is studied in the frequency domain using signal theory tools to unveil its underlying characteristics. In this regard, we observe that although some works analyze the spectral characteristics of OCDM [2], [3], [32], none have delved into the consequences of aliasing that occurs when generating an OCDM signal by exploiting the IDFnT. This phenomenon is mentioned only in [2], which, however, does not provide a thorough analytical investigation as to why numerically-generated OCDM signals, despite being subject to aliasing distortion, can still be efficiently demodulated.

In this paper, instead, we analytically investigate the spectral properties of OCDM, showing that exploiting the IDFnT for its generation introduces both inter-chirp and intra-chirp interference, which compromise the signal integrity. We also provide, however, the analytical demonstration that such interfering contributions are not preventing the successful demodulation of the signal and, on the contrary, have a beneficial effect. To the best of our knowledge, this aspect, analytically investigated in Section II, has not been previously tackled in the existing literature, thus constituting the first novel contribution of this paper.

Regarding the performance provided by OCDM, a thorough analysis is presented in [5], where the BER is investigated by also taking into account a possible Carrier Frequency Offset (CFO) induced by, e.g., oscillator mismatch, as well as time-burst and narrowband interference. In contrast to [5], which assumes a constant CFO, our paper considers random, time-variant phase variations induced by PN. Specifically, we account for time-correlated phase variations originating from PLL-based oscillators, carefully modeling the statistics and spectral characteristics of PN expected in the THz band. Additionally, along with Inter Carrier Interference (ICI), we also address the impact of Common Phase Error (CPE), the latter being assumed perfectly compensated in [5]. Additionally, [5] considers the 3GPP Extended Vehicular A (EVA) channel model, which is targeted to E-UTRA bands not exceeding 6 GHz. As, such, no insight is provided in [5] regarding the distinctive features of THz communications as well as the performance of OCDM at these high frequencies. In contrast, since beyond-5G systems are also expected to operate in the THz band, in this paper, we make an initial assessment of the performance of OCDM in this frequency range, comparing it with the well-established OFDM modulation.

Specifically, as discussed above, we consider the PN, as it is well known that oscillators are affected by this phenomenon at such a high frequency, which impacts communication reliability. In particular, we take as a reference a real oscillator working at 237.7 GHz [33]. In addition, to adequately model the presence of molecular noise and thermal noise in our investigations, we thoroughly discuss their characteristics in the considered frequency range. To the best of the authors' knowledge, this is the first paper that addresses the performance of OCDM in the THz band, which means taking into careful consideration the specific disturbances that play a significant role in this region of the electromagnetic spectrum.

This investigation, carried out through a simulative approach and outlined in Sections III and IV, represents the second original contribution presented in this manuscript.

II. OCDM: SIGNAL ANALYSIS

The fundamental principle underpinning OCDM is the simultaneous transmission of mutually orthogonal chirp waveforms with overlapping spectra, each of which is modulated by an M-ary modulation symbol. Accordingly, the complex envelope of an OCDM signal can be written as

$$i(t) = \sum_{n} \sum_{k=0}^{N-1} x_k(n) \psi_k(t - nT) g_T(t - nT) \tag{1}$$

where

- the index n refers to the n-th symbol interval of duration T,
- $\psi_k(t)$ represents the k-th chirp waveform within a set of N mutually orthogonal chirp waveforms denoted by $\Psi = \{\psi_k(t)\}_{k=0}^{N-1}$,
- $N = |\Psi|$ is the number of orthogonal chirp waveforms in Ψ,
- $x_k(n)$ is the complex M-QAM modulation symbol transmitted in the n-th symbol interval by the k-th chirp waveform,
- $g_T(t)$ is the indicator function, that is, $g_T(t) = 1$ for $0 \leq t < T$, and $g_T(t) = 0$ elsewhere.

Specifically, the set Ψ of N (complex) orthogonal chirps is given by [2]:

$$\Psi = \{\psi_k(t)\}_{k=0}^{N-1} = \{e^{j\frac{\pi}{4}} e^{-j\pi \frac{B}{T}\left(t-\frac{k}{B}\right)^2}\}_{k=0}^{N-1} \quad (2)$$

with B defined as follows:

$$B \triangleq \frac{N}{T}. \quad (3)$$

Given (1), it results that N modulation symbols $[x_0(n), x_1(n), \ldots, x_{N-1}(n)]$ are transmitted by means of N orthogonal chirp waveforms in the n-th time interval of duration T. In the following, we will use the term "OCDM symbol interval" when referring to T.

The time evolution of the generic chirp $\psi_k(t)$ can be studied by deriving its instantaneous frequency deviation. In particular, given

$$\psi_k(t) = e^{j\frac{\pi}{4}} e^{-j\pi \frac{B}{T}\left(t-\frac{k}{B}\right)^2} \quad (4)$$

$$= e^{j\theta_k(t)} \quad k \in [0, 1, \ldots N-1], \quad (5)$$

it follows that the instantaneous frequency deviation of the k-th chirp is

$$\Delta f_k(t) = \frac{1}{2\pi}\frac{d\theta_k(t)}{dt} = \frac{k}{T} - \frac{B}{T}t. \quad (6)$$

As it turns out, the instantaneous frequency deviation of the complex OCDM chirp $\psi_k(t)$ covers an interval B in the time period $[0, T)$, gradually decreasing in a linear fashion from $\frac{k}{T}$ to $\frac{k}{T} - B$. As an example, the spectrogram of a family of $N = 8$ complex chirps is shown in Fig. 1(a) in the case $T = 1$ ms.

Remark: As previously mentioned, the value B of the frequency sweep interval cannot be chosen independently of other modulation parameters, as it is related to the OCDM symbol duration T and the number of chirps N by (3). In fact, the constraint posed by (3) is the basis for the generation and the demodulation of OCDM signals by means of numerical techniques, as well as for their spectral characteristics. These issues will be discussed in the following sections.

A. SPECTRUM OF A COMPLEX LINEAR CHIRP

To investigate the spectral properties of chirps, we computed the Fourier transform of the generic, k-th, complex chirp within the interval $[0, T)$ (see Appendix A):

$$\Psi_k(f) = \mathcal{F}\left[\psi_k(t) g_T(t)\right] = \mathcal{F}\left[e^{j\frac{\pi}{4}} e^{-j\pi \frac{B}{T}\left(t-\frac{k}{B}\right)^2} g_T(t)\right] = e^{j\frac{\pi}{4}} \frac{e^{j\pi\frac{f^2}{\gamma}} e^{-j2\pi f\frac{k}{B}}}{\sqrt{2\gamma}} \left[\mathrm{C}\left(\sqrt{2\gamma}\left(T-\frac{k}{B}\right)+\sqrt{\frac{2}{\gamma}}f\right)\right.$$

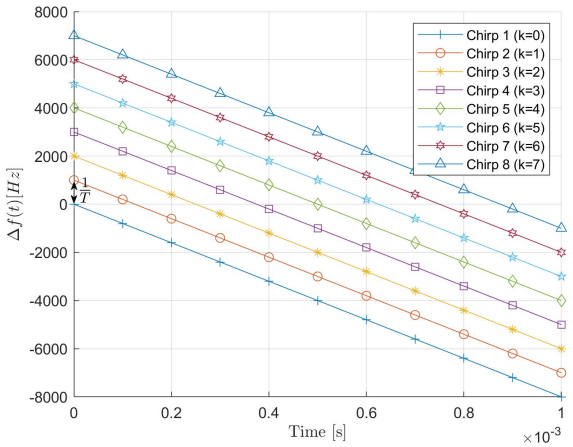

(a) Frequency deviation as a function of time for $N = 8$ chirps and $T = 1$ ms, which (recalling (3)) gives $B = 8$ kHz.

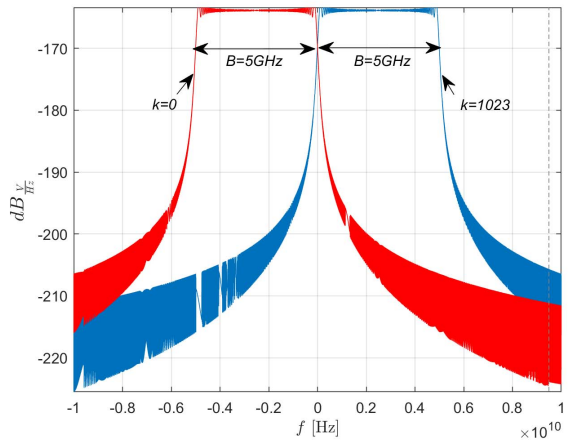

(b) Chirp spectra for $k = 0$ (leftmost plot), and $k = 1023$ (rightmost plot). We set B = 5 GHz, $N = 1024$, and consequently $T = 2.048 \cdot 10^{-7}$s.

FIGURE 1. Chirps' characterization.

$$\left. - \mathrm{C}\left(-\sqrt{2\gamma}\frac{k}{B}+\sqrt{\frac{2}{\gamma}}f\right) - j\mathrm{S}\left(\sqrt{2\gamma}\left(T-\frac{k}{B}\right)+\sqrt{\frac{2}{\gamma}}f\right) + j\mathrm{S}\left(-\sqrt{2\gamma}\frac{k}{B}+\sqrt{\frac{2}{\gamma}}f\right)\right]. \quad (7)$$

where $\mathcal{F}[\cdot]$ is Fourier transform operator, $C(z) \triangleq \int_0^z \cos(\frac{\pi t^2}{2})\, dt$ is the Fresnel cosine integral function, $S(z) \triangleq \int_0^z \sin(\frac{\pi t^2}{2})\, dt$ is the Fresnel sine integral function[2] and $\gamma = \frac{B}{T}$.

As an example case, Fig. 1(b) shows $|\Psi_k(f)|$, that is, the amplitude spectrum of $\psi_k(t) g_T(t)$ for $k = 0$ (leftmost

2. A similar expression is reported in [3]. It refers, however, only to the basic chirp, corresponding to $k = 0$. In this paper, instead, we need the Fourier transforms of all chirps, that is, for $0 \le k \le N-1$. This is why we derived the general expression appearing in (7).

plot) and $k = 1023$ (rightmost plot) in the case $N = 1024$, $B = 5$ GHz[3] and, consequently, $T = \frac{N}{B} = 2.048 \cdot 10^{-7}$ s. For intermediate values of k, the spectra of the corresponding chirps fall between the two extreme cases represented in Fig. 1(b).[4]

Observing the figure, it is worth noting that the N chirp waveforms of an OCDM signal collectively span a frequency range of approximately $2B$.

B. IDFnT-BASED IMPLEMENTATION OF OCDM SIGNALS

Let us focus the attention on the complex envelope (1) of OCDM signals in the generic n-th symbol interval:

$$i_n(t) = \sum_{k=0}^{N-1} x_k(n) e^{j\frac{\pi}{4}} e^{-j\pi \frac{B}{T}\left(t-nT-\frac{k}{B}\right)^2} g_T(t-nT). \quad (8)$$

To simplify the notation, without loss of generality, hereafter we consider the expression (8) for $n = 0$, thus assuming $[0, T)$ as the reference OCDM symbol interval. Moreover, for the sake of conciseness, we also denote $x_k(0) = x_k$:

$$i_0(t) = \sum_{k=0}^{N-1} x_k e^{j\frac{\pi}{4}} e^{-j\pi \frac{B}{T}\left(t-\frac{k}{B}\right)^2} g_T(t). \quad (9)$$

Taking N samples of (9), where N is an even number, evenly spaced by T_s within the reference interval $[0, T)$, corresponds to assuming a sampling rate $f_s = \frac{1}{T_s} = \frac{N}{T}$ and designate the sampling instants as $t_l = lT_s$, where $l = (0, 1, \ldots, N-1)$. This yields the following discrete-time signal:

$$\begin{aligned} i_0(t_l) &= \sum_{k=0}^{N-1} x_k e^{j\frac{\pi}{4}} e^{-j\pi \frac{B}{T}\left(t_l-\frac{k}{B}\right)^2} g_T(t_l) \\ &= \sum_{k=0}^{N-1} x_k e^{j\frac{\pi}{4}} e^{-j\pi \frac{B}{T}\left(l\frac{T}{N}-\frac{k}{B}\right)^2} g_T\left(l\frac{T}{N}\right) \\ &= e^{j\frac{\pi}{4}} \sum_{k=0}^{N-1} x_k e^{-j\pi \frac{B}{T}\frac{T^2}{N^2}\left(l-\frac{k}{B}\frac{N}{T}\right)^2} g_T\left(l\frac{T}{N}\right) \\ &\quad \text{with } l = 0, 1, \ldots, N-1. \end{aligned} \quad (10)$$

By recalling (3), (10) can be further elaborated as

$$\begin{aligned} i_0(t_l) &= e^{j\frac{\pi}{4}} \sum_{k=0}^{N-1} x_k e^{-j\frac{\pi}{N}(l-k)^2} g_T\left(l\frac{T}{N}\right) \\ &\quad \text{with } l = 0, 1, \ldots, N-1. \end{aligned} \quad (11)$$

Given the definition of $g_T(t)$, the samples of the complex envelope in the considered OCDM symbol interval can be finally expressed as:

$$i_0(t_l) = e^{j\frac{\pi}{4}} \sum_{k=0}^{N-1} x_k e^{-j\frac{\pi}{N}(l-k)^2} \text{ with } l = 0, 1, \ldots, N-1. \quad (12)$$

Remarkably, (12) is also the definition of the IDFnT of the sequence $\{x_k\}_{k=0}^{N-1}$ when N is even, thus showing that the IDFnT is the straightforward mathematical tool for the generation of discrete-time OCDM signals. Extending the analysis to the case where N is odd is straightforward, with minor modifications, and for this reason we avoid reporting its expression.

It is important to note that (12) is not a novel result, having been previously derived in [2]. However, we decided to reintroduce its full derivation to better focus the reader's attention on two mathematical steps that are of great importance for the analysis presented in the following sections. First, (11) follows from (10) only by setting $BT = N$, which constrains the value of B once N and T are fixed (see (3)). Second, the fundamental equation (12) is obtained only on condition that the sampling frequency is $f_s = \frac{N}{T}$ that, given the above constraint on B, leads to $f_s = B$. This constraint on f_s, which we wanted to emphasize, does not come without consequences, as will be shown in the following sections.

C. ON THE INTEGRITY OF OCDM SIGNALS GENERATED THROUGH THE IDFnT

As pointed out in Section II-B, by means of the IDFnT expressed in (12), one can derive N equally spaced samples of the OCDM complex envelope in $[0, T)$ starting from the N modulation symbols $\{x_k\}_{k=0}^{N-1}$ to be transmitted in the same interval of time. As observed in the previous section, this requires $f_s = \frac{N}{T}$ and thus, given (3), $f_s = B$. Notably, this condition on f_s gives rise to issues pertaining to signal integrity, also impacting on its bandwidth, which will be investigated hereafter.

In particular, in Section II-B, we introduced the complex envelope $i_n(t)$ of an OCDM signal in the generic n-th OCDM symbol interval (see (8)), whose spectrum spans (and exceeds) the frequency interval $[-B, B]$, as evident in Fig. 1(b). In a conventional (that is, non IDFnT-based) transmitter, the real (in-phase) and imaginary (quadrature) components of $i_n(t)$ would be supplied to a quadrature modulator for the Radio-Frequency (RF) upconversion, as shown in Fig. 2(a). Clearly, the quadrature modulator operates by performing a frequency translation of the signal's spectrum, thereby aligning it with the carrier frequency f_0, while preserving its original shape and, consequently, originating an RF signal with a bandwidth (approximately) equal to $2B$.

However, according to the IDFnT-based signal-generation strategy outlined in Section II-B, the baseband numerical modulator depicted in Fig. 2(b) is not expected to output the continuous-time signal (8), but, rather, its samples (12) with a sampling rate $f_s = B$. Recalling that the spectrum of (8) spans (and exceeds) the interval $[-B, B]$, it immediately turns out that the condition on the minimum sampling rate f_s

3. Such value is quite common at THz frequencies; for instance, the IEEE 802.15.3d standard foresees eight different frequency intervals between 2.16 GHz and 69.12 GHz for carrier frequencies belonging to the interval [252, 325] GHz [34].

4. As expected, the spectra depicted in Fig. 1(b) do not show Hermitian symmetry, as they are the results of the Fourier transforms of complex signals.

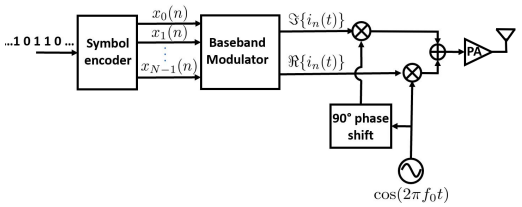

(a) OCDM synthesis based on the continuous-time baseband representation.

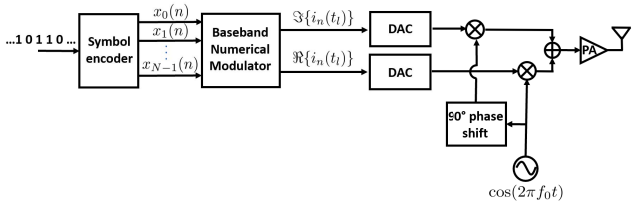

(b) OCDM synthesis based on the discrete-time baseband representation.

FIGURE 2. **OCDM synthesis based on continuous-time (a) or discrete-time (b) baseband representations. Symbols and signals refer to the *n*-th chirp interval, and the triangle labelled PA represents the power amplifier.**

dictated by the sampling theorem is not fulfilled. The obvious consequence is that the Digital-to-Analog Conversion (DAC) of the real and imaginary parts of (12) generates continuous-time signals (namely, the DACs' outputs in Fig. 2(b)) that are certainly distorted with respect to the real and imaginary parts of (8), owing to the unavoidable aliasing in the frequency domain.

It results that generating OCDM signals using numerical techniques that leverage the IDFnT makes the transmitted signal so distorted, compared to the simple sum of orthogonal chirps expressed by (8), that one might expect the orthogonality of the chirps to be irreparably compromised. In the following subsections, we will employ a signal-theoretic approach to elucidate why the distortion caused by aliasing does not impede the retrieval of transmitted symbols at the receiver side. This will establish the theoretical foundations that establish the IDFnT as a viable and convenient solution for the numerical generation of OCDM signals.

D. IDFnT-BASED OCDM: INTER-CHIRP AND SELF-CHIRP INTERFERENCE

Let us focus our attention, first, on a generic chirp $\psi_k(t)$ in the symbol interval $[0, T)$. Its spectrum $\Psi^{(k)}(f)$, given by (7), is mostly (but not entirely) contained in a frequency interval of width B, as evident in Fig. 1(b).

Given $\Psi^{(k)}(f)$, it is well known that the discrete-time signal consisting of the samples of $\psi_k(t)$ taken with rate $f_s = B$ in the interval $[0, T)$ has the following spectrum [35]

$$\Psi_s^{(k)}(f) = B \sum_{m=-\infty}^{\infty} \Psi_k(f - mB), \tag{13}$$

which is periodic with period B. Clearly, (13) is affected by aliasing, resulting from undersampling. In this regard, Fig. 3(a) and Fig. 3(b) show some of the periodic repetitions $|\Psi_k(f - mB)|$ and $|\Psi_i(f - mB)|$, with $m \in \mathbb{Z}$ denoting the

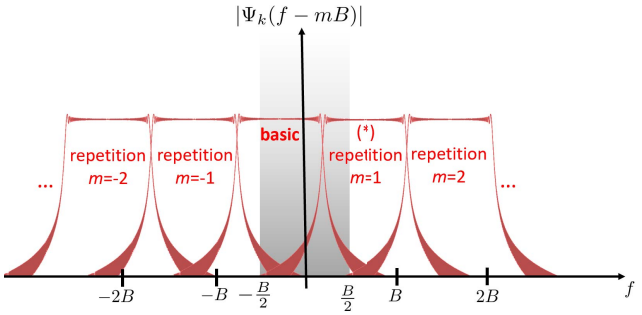

(a) Periodic repetition of the spectrum of a given chirp k.

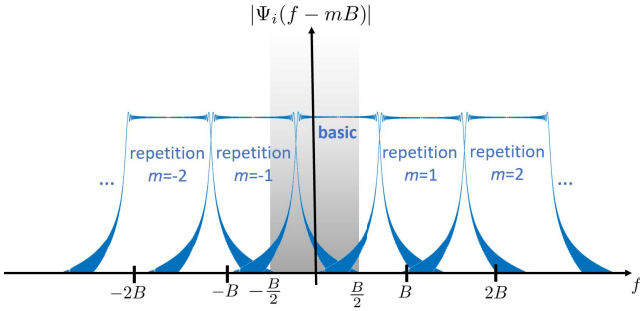

(b) Periodic repetition of the spectrum of a given chirp i, with $i > k$.

FIGURE 3. **Periodic repetitions of the spectrum of two different chirps.**

repetition index, pertaining to the generic k-th and i-th chirp, respectively, with $i > k$.

In the figures, we deliberately did not represent the amplitude spectra $|\Psi_s^{(k)}(f)|$ and $|\Psi_s^{(i)}(f)|$ for the two sampled chirps, although it would seem logical to do so. Instead, we directed our focus towards the amplitude spectrum of each repetition, specifically $|\Psi_k(f - mB)|$ and $|\Psi_i(f - mB)|$, to better appreciate to which extent it overlaps with the adjacent ones. To ensure clarity in the figures, the basic spectrum of the chirp, corresponding to $m = 0$, as well as its repetitions, are clearly labeled.

When observing Fig. 3, there are two aspects that are worth emphasizing:

- *A1:* Irrespectively of the specific chirp considered (that is, regardless of whether one looks at Fig. 3(a), which refers to chirp k, or Fig. 3(b), which refers to chirp i), the aliasing phenomenon at the boundaries of each spectrum repetition is clearly evident, as expected.
- *A2:* The spectrum repetitions pertaining to the sampled k-th chirp overlap also with the basic spectrum (and its repetitions) of any other chirp i (with $i \neq k$). This is evident in Fig. 3, where it clearly appears that the spectrum repetition labeled with the symbol (*) in Fig. 3(a), which pertains to chirp k, is partially overlapped with the basic spectrum of the i-th chirp, shown in Fig. 3(b).

Comment: An OCDM signal that is generated as depicted in Fig. 2(a), that is, through the quadrature modulation of the continuous-time in-phase and quadrature components of (8), is intrinsically made by the sum of chirps whose spectra (the basic spectra in Figs. 3(a) and 3(b)) are partially overlapped,

which entails that inter-chirp interference is introduced in the frequency domain. Their orthogonality in the time domain allows, however, to discriminate one chirp from another.

On the other hand, using numerical techniques that leverage the IDFnT to generate OCDM signals, as envisioned in Fig. 2(b), introduces further interference contributions, namely a self-chirp interference contribution (see A1) as well as an additional inter-chirp interference contribution (see A2). Clearly, this means that the shape of the OCDM signal obtained through the modulator shown in Fig. 2(a) is completely different from that obtained through the modulator depicted in Fig. 2(b).

E. ON THE BANDWIDTH OF THE TRANSMITTED OCDM SIGNAL

Having in mind the numerical architecture shown in Fig. 2(b), in Fig. 3 we plotted grey boxes to highlight the frequency interval $[-\frac{B}{2}, \frac{B}{2}]$ that contains the spectra of the signals generated by the DACs. In fact, given the choice $f_s = B$, any spectral component of the discrete-time signal that falls outside the $[-\frac{B}{2}, \frac{B}{2}]$ interval is filtered out by the DACs themselves to generate the continuous-time signals. Clearly, the quadrature modulation of the DACs' outputs generates an RF signal whose bandwidth is equal to B, which is half the bandwidth of the RF signal obtained through the modulator depicted in Fig. 2(a).

It turns out that generating OCDM signals using numerical techniques that leverage the IDFnT, makes the transmitted signal so distorted, compared to the simple sum of orthogonal chirps expressed by (8), that even its bandwidth is half than expected.

F. OCDM DEMODULATION THROUGH THE DISCRETE FRESNEL TRANSFORM

It is well-known that OCDM signals generated by means of the IDFnT can be demodulated through the Discrete Fresnel Transform (DFnT) of the (complex) signal samples that result from the analog-to-digital conversion of the in-phase and quadrature components of the received signal. Given the distortion introduced by the undersampling, one may wonder what are the theoretical foundations that make it possible to recover the transmitted symbols.

In this regard, let us assume that perfect carrier and symbol synchronization is achieved at the receiver side. Once the received signal is converted to the baseband and sampled with the same rate used at the transmitter side, that is $f_s = B$, the spectral repetitions depicted in Fig. 3 are restored as well as the self-chirp and inter-chirp interference. Let us consider, now, the generic m-th spectral component of the k-th chirp shown in Fig. 3(a), either basic o repeated. In the time domain, it would correspond to a continuous-time chirp given by:

$$\psi_k^{(m)}(t) = e^{j\frac{\pi}{4}} e^{-j\pi\frac{B}{T}\left(t-\frac{k}{B}+mT\right)^2} \quad \text{with } m \in \mathbb{Z}. \tag{14}$$

The reader can refer to Appendix B for the proof of (14).

Having obtained the time-domain representation (14) of each spectrum component, responsible of both self-chirp and inter-chirp interference, we can now demonstrate that each chirp of the basic set (2) is orthogonal[5] to (14) in $[0, T)$. To this aim, let us define the inner product between complex functions in the interval $[0, T)$ as

$$\langle f, g\rangle \triangleq \int_0^T f(t)g^*(t)dt \tag{15}$$

with $g^*(t)$ denoting the complex conjugate of $g(t)$. As it is evident, the orthogonality between two functions can be assessed by deriving their inner product. Therefore, focusing the attention on the generic chirp $\psi_k(t)$ belonging to the basic set (2) and $\psi_i^{(m)}(t)$, we investigate their orthogonality by deriving:

$$\begin{aligned}\langle \psi_k(t), \psi_i^{(m)}(t)\rangle &= \int_0^T \psi_k(t)\left[\psi_i^{(m)}(t)\right]^* dt \\ &= T\,\mathrm{sinc}\Big(k-i+mN\Big)\cdot e^{j\pi\frac{(i^2-k^2)}{N}} \\ &\quad \cdot e^{j\pi Nm^2} e^{j\pi(k-i+mN)}.\end{aligned} \tag{16}$$

where:

$$\mathrm{sinc}(x) \triangleq \begin{cases} \frac{\sin(\pi x)}{\pi x} & \text{for } x \neq 0 \\ 1 & \text{for } x = 0. \end{cases} \tag{17}$$

The proof of (16) can be found in Appendix C. Given (16), it turns out that:

- when $i = k$ with $i \in \{0, 1, \ldots, N-1\}$ and $m \in \mathbb{Z}\backslash 0$, which means that we are considering self-chirp interference contributions, it is $\langle \psi_k(t), \psi_k^{(m)}(t)\rangle = 0$.
- when $i \neq k$, which means that we are considering inter-chirp interference contributions, it is $\langle \psi_k(t), \psi_i^{(m)}(t)\rangle = 0$.

Notably, it can be inferred that each chirp in the basic set (2) is orthogonal to all interference contributions within the interval $[0, T)$. One observes, by the way, that letting $i = k$ and $m = 0$ in (16), which means computing the inner product of one chirp by itself since $\psi_k^{(0)}(t) = \psi_k(t)$, yields $\langle \psi_k(t), \psi_k(t)\rangle = T$, as expected.

G. COMMENTARY

The novel analytical results presented in Sections II-C–II-F demonstrate that the self-chirp interference and inter-chirp interference resulting from undersampling, although causing distortions, do not compromise the demodulation process of OCDM signals. On the contrary, they translate into a benefit as the RF bandwidth of an OCDM signal generated using numerical techniques leveraging the IDFnT, by means of the scheme depicted in Fig. 2(b), is halved compared to the bandwidth of an OCDM signal generated based on the continuous-time representation of baseband signals using the scheme in Fig. 2(a).

5. Provided that the two chirps considered are not, actually, the same chirp.

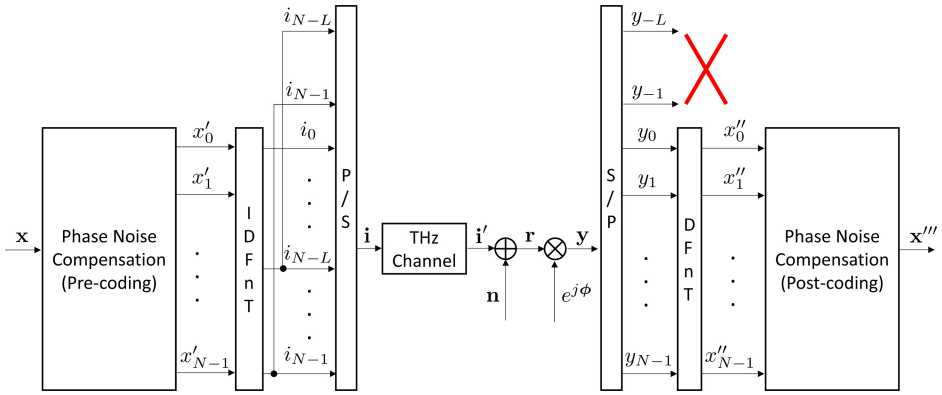

FIGURE 4. Discrete-time low-pass equivalent model of the considered OCDM system.

III. SYSTEM MODEL

After thoroughly analyzing the nature of an OCDM signal from its fundamentals, in the remaining part of this article we investigate the performance of an OCDM link operating at THz frequencies, also drawing comparisons to an OFDM system considered as a benchmark. Specifically, in this section we present the discrete-time simulator we implemented to investigate an OCDM link (transmitter + channel + receiver) operating in the THz band, providing details about its block scheme, the processing it performs, and the models it incorporates, whereas, Section IV will provide the corresponding outcomes. Importantly, the description of the OCDM simulator provided in this section also applies to the simulator of the benchmark OFDM system, with the only difference being the Fourier transform-based modulation/demodulation part, which will not be further elaborated for conciseness.

It is worth emphasizing that when investigating the performance of communication systems operating at such high frequencies, either analytically or by simulation, some aspects peculiar to the THz band must be carefully considered. First, making accurate oscillators for transceivers working at THz frequencies is a major problem today, as they exhibit significant PN that has a detrimental impact on communication and cannot be disregarded in the investigation. Moreover, in addition to the thermal noise, a further noise source must be considered, namely, the molecular noise. In this regard, particular attention must be paid to the spectral characteristics of both thermal and molecular noises, which are highly distinctive in the THz frequency range.

In the following, after introducing the IDFnT-based OCDM system under investigation, we present the PN model we considered, and we discuss how molecular and thermal noises have been taken into account.

A. THE CONSIDERED OCDM SYSTEM

The discrete-time low-pass equivalent model of the investigated system is shown in Fig. 4, which provides both the reference scheme for the following discussions and a pictorial representations of the main components of our simulator.

Given the array $\mathbf{x}$ of M-QAM complex symbols to be transmitted in the n-th OCDM symbol interval, a pre-coding operation is performed to facilitate the mitigation, at the receiver side, of the PN introduced along the communication path. Then, the array $\mathbf{x}' = [x'_0, x'_1, \ldots, x'_{N-1}]$ of N pre-coded symbols undergoes the IDFnT processing, resulting in a set of N complex samples of $i_n(t)$ that are collected in the array $\mathbf{i_N} = [i_0, i_1, \ldots, i_{N-1}]$.

Starting from $\mathbf{i_N}$, to deal with the possible frequency-selective nature of the channel, the transmitter inserts a cyclic prefix of length L to obtain the array $\mathbf{i}$, that represents, ultimately, the discrete-time (low-pass equivalent) signal to be transmitted in the current OCDM symbol interval (see Fig. 4). After the parallel-to-serial conversion, the signal samples are then passed to the THz channel, which, in our case, can be either a single- or multi-path channel, and, in the latter case, we resort to the small-scale α-μ fading model [36]. The resulting vector, named $\mathbf{i}'$, is then corrupted by the additive noise, represented in Fig. 4 by $\mathbf{n}$, which includes both the thermal noise and the molecular noise. The two noise contributions deserve, however, a separate discussion, as their spectra are not flat at such high frequencies: their characteristics and the assumptions adopted in our discrete-time simulator are discussed in Appendix D and Appendix E.

As evident in Fig. 4, the system being analyzed also takes into account the presence of PN, which is introduced through the multiplicative term $e^{j\boldsymbol{\phi}}$. In particular, $\boldsymbol{\phi}$ denotes the array of correlated discrete-time phase fluctuations, whose model will be discussed in the following section. At the receiver side, assuming perfect time and frequency synchronization, the received signal at instant p is thus expressed by [37]:

$$y_p = i'_p e^{j\phi_p} + n_p, \tag{18}$$

where i'_p is the complex envelope of the signal at the output of the THz channel at instant p, while ϕ_p and n_p are the oscillator PN and the additive noise in the same instant, respectively.

The receiver then performs the serial-to-parallel conversion, removes the cyclic prefix and applies the DFnT to

demodulate the signal. The l-th output of the DFnT in the current symbol interval is, therefore:

$$x_l'' = \frac{1}{N}\sum_{k=0}^{N-1} y_k e^{-j\frac{\pi}{4}} e^{j\frac{\pi}{N}(l-k)^2}, \text{ with } l = 0, 1, \ldots, N-1. \tag{19}$$

Clearly, the DFnT output is impaired by both the PN and the additive noise, which produce different effects that are worth highlighting. In particular, by inserting (12) and (18) in (19), it is possible to write:

$$x_l'' = \frac{1}{N}\sum_{k=0}^{N-1}\left(e^{j\frac{\pi}{4}}\sum_{r=0}^{N-1} x_r e^{-j\frac{\pi}{N}(k-r)^2} e^{j\phi_k} + n_k\right)\cdot e^{-j\frac{\pi}{4}} \cdot \cdot e^{j\frac{\pi}{N}(l-k)^2}, \text{ with } l = 0, 1, \ldots, N-1, \tag{20}$$

which, after simple manipulations, becomes:

$$x_l'' = x_l \frac{1}{N}\sum_{k=0}^{N-1} e^{j\phi_k} + \frac{1}{N}\sum_{\substack{r=0\\ r\neq l}}^{N-1} x_r \sum_{k=0}^{N-1} e^{j\phi_k} e^{-j\frac{\pi}{N}(r-l)(r+l-2k)} + + \frac{1}{N}\sum_{k=0}^{N-1} n_k e^{-j\frac{\pi}{4}} e^{j\frac{\pi}{N}(l-k)^2}, \text{ with } l = 0, 1, \ldots, N-1. \tag{21}$$

Equation (21) highlights the two main effects of PN on OCDM signals. On one hand, all M-QAM symbols transmitted in the same OCDM symbol interval undergo a phase rotation, which is common to all of them. This is the so-called CPE, which appears in the first term of (21). On the other hand, PN also undermines the orthogonality of chirps, causing M-QAM symbols associated with different chirps to interfere with each other. This effect is known as ICI, and is expressed by the second term of (21). The third term of (21) originates, instead, from the DFnT of the additive noise samples.

Both CPE and ICI are clearly evident in Fig. 5 (see the red empty dots), which depicts an example of received constellation corresponding to a 4-QAM OCDM signal impaired solely by PN. Specifically, the rotation of the constellation is caused by CPE, while the deviation of the actual points from the ideal modulation symbols is the effect of the ICI.

To mitigate the impact of PN, the receiver being considered incorporates a post-coding stage that outputs the array $\mathbf{x}'''$ of recovered modulation symbols, which are subsequently processed by the simulator to evaluate the system's performance.[6] Specifically, the numerical results presented in Section IV have been obtained by employing the pre-coding and post-coding techniques described in [39], which aim to compensate for both CPE and ICI within each OCDM symbol interval. Hereafter, we will refer to the application of such an algorithm as *"PN compensation"*. In Fig. 5, the effect of this PN compensation algorithm on the received constellation can also be observed (see the blue solid dots).

6. It is worth noting that the receiver does not perform any equalization procedure after performing the DFnT. This choice follows from the consideration that the α-μ fading, that characterizes the propagation in the THz band, is frequency flat. More details on this aspect can be found in [38].

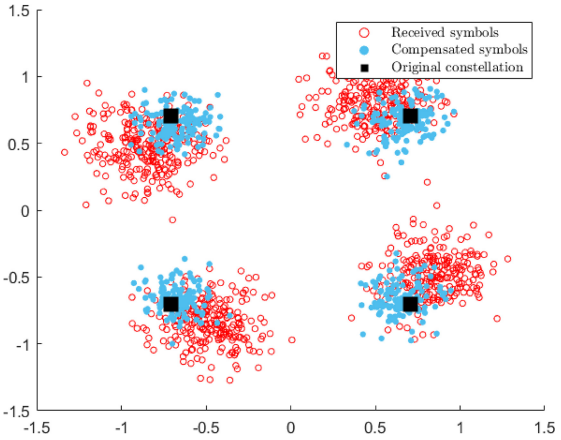

FIGURE 5. Constellation of a 4-QAM OCDM signal impaired by the PN and considering the two cases where the PN compensation algorithm proposed in [39] is applied or not.

B. PHASE NOISE MODEL

In Section III-A, to avoid diverting from the main topic of that section (which was the system architecture), we did not provide any detail about the PN model we adopted. This gap is filled below, where the PN is introduced, and the model adopted in our investigation is presented.

As is known, the ideal output of an oscillator is a sine wave $v(t) = V_0 \sin(2\pi f_0 t + \phi)$, whose one-sided spectrum is an impulse at frequency f_0. Unfortunately, the output of practical oscillators exhibits unwanted amplitude and phase fluctuations, hence it can be more generally expressed as

$$v(t) = V(t)\sin\big[2\pi f_0 t + \phi(t)\big]. \tag{22}$$

While amplitude fluctuations can be practically eliminated by applying a limiter to the oscillator output, phase fluctuations cannot be mitigated just as easily, thus making the spectrum of $v(t)$ extend around f_0 and, ultimately, giving rise to PN.

Indeed, one of the main challenges for the realization of THz communication systems is to equip transceivers with high-frequency oscillators featuring low PN. This goal is usually pursued by means of PLL circuits, which are used to lock the output of a voltage-controlled oscillator (VCO) to a reference (very stable) input signal, thus making the oscillator's output as accurate as the reference input [33], [40], [41].

However, although more accurate than free-running oscillators, PLLs exhibit PN as well. In particular, when the oscillator is subject to white noise, the PN is given by the superposition of a cumulative Wiener process (i.e., a one-dimensional, continuous-time, Gaussian random walk) and an uncorrelated Gaussian process. The former, having

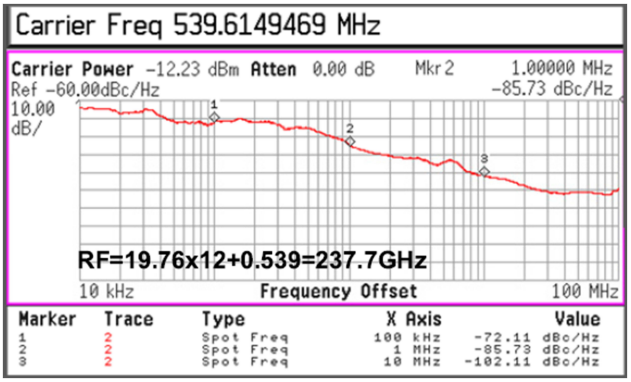

(a) PN spectrum of the PLL-based frequency synthesizer working at 237.7 GHz that we consider in this paper. This figure was taken from [33].

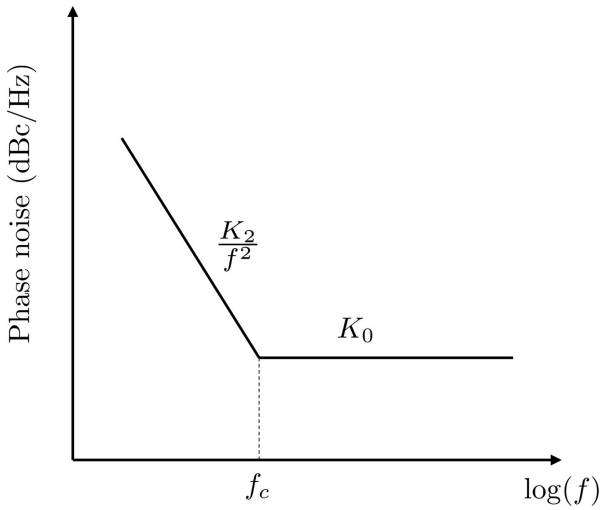

(b) Model of the PN spectrum at 237.7 GHz corresponding to the PLL proposed in [33].

FIGURE 6. PN characteristics.

a Lorentzian (i.e., $1/f^2$) spectrum [42], results from the integration of the white noise within the PLL, whereas the latter is caused by its amplification, being thus characterized by a white spectrum [37], [43].

In this regard, Fig. 6(a) shows the Power Spectral Density (PSD) of the PLL-based frequency synthesizer working at 237.7 GHz that we consider in this paper [33]. Specifically, the coloured part of the spectrum (decreasing with the frequency) is clearly evident, as is the flat (i.e., white) part, which begins at about 30 MHz. This shape is usually modelled as shown in Fig. 6(b), that is, by means of two parameters, namely K_2 and K_0, which give the slope of the power spectral density of the Wiener PN and the power spectral density of the uncorrelated (i.e., white) part of the spectrum, respectively [37].

Since the considered PN is the superposition of a cumulative Wiener process and an uncorrelated Gaussian process, in our simulator the p-th PN sample is given by

$$\phi_p = \phi_{w,p} + \phi_{g,p}, \tag{23}$$

where:

- $\phi_{g,p} \sim \mathcal{N}(0, \sigma_g^2)$ represents the uncorrelated Gaussian PN at instant p, with $\sigma_g^2 = K_0 B$ [37];
- $\phi_{w,p}$ represents the Wiener PN at instant p and is given by $\phi_{w,p} = \phi_{w,p-1} + \delta\phi_{w,p}$, with $\delta\phi_{w,p} \sim \mathcal{N}(0, \sigma_w^2)$, $\sigma_w^2 = 4\pi^2 K_2 T_s$ [37], [42].

Having in mind Fig. 6(b), it is worth observing that the variances σ_g^2 and σ_w^2 are bonded by the corner frequency $f_c = \sqrt{K_2/K_0}$, whose impact on the communication performance will also be investigated.

IV. NUMERICAL RESULTS

This section presents the results of our investigation into the performance of an OCDM system impaired by PN at THz frequencies. Additionally, the performance of OFDM under the same conditions is also reported for the sake of comparison. The simulator employed for this analysis undergoes cyclic iterations, simulating the OCDM communication link depicted in Fig. 4, until a predetermined number of errors (threshold) on the received bits is attained. For the lowest BER encountered in our simulations (approximately 10^{-8}), this threshold was set to 200 errors. For higher values of the BER, the error threshold was increased to further enhance accuracy.

To model the PN, we considered as a reference the oscillator described in [33], which was designed to operate at 237.7 GHz. The corresponding PN spectrum, shown in Fig. 6(a), was modeled as illustrated in Fig. 6(b). In particular, comparing Fig. 6(a) and Fig. 6(b), it clearly appears that, for this oscillator, it is $f_c = 30$ MHz, and $K_0 = -110$ dBc/Hz. These values, along with those in their vicinity, served as references for our investigation. As anticipated in Section III-A, the numerical results presented in the following were obtained considering the PN compensation algorithm proposed in [39].

Of course, the presence of the additive noise, which includes both thermal and molecular noise (modelled as discussed in Appendix D and Appendix E) was also taken into account. More precisely, the performance figure investigated in the following, namely the BER, has been evaluated considering its dependence also on the SNR, which is defined as the ratio between the received signal power and the noise power within the bandwidth B.

The analysis starts with Fig. 7, which is composed of four plots showing the BER as a function of the SNR for both OCDM and OFDM systems. The impact of three key parameters, namely K_0, f_c, and N, was examined, along with the role played by PN compensation and different modulation orders.

In particular, Fig. 7(a) was obtained by considering a 4-QAM modulation and setting $N = 1024$, $B = 5$ GHz, $f_c = 30$ MHz. K_0 is instead taken in the set $\{-100, -110\}$ dBc/Hz, in accordance with the characteristics of the reference oscillator presented in [33].

First, it is evident that a precise alignment exists between the simulated and analytical curves for both the OCDM and OFDM schemes when considering only Additive White

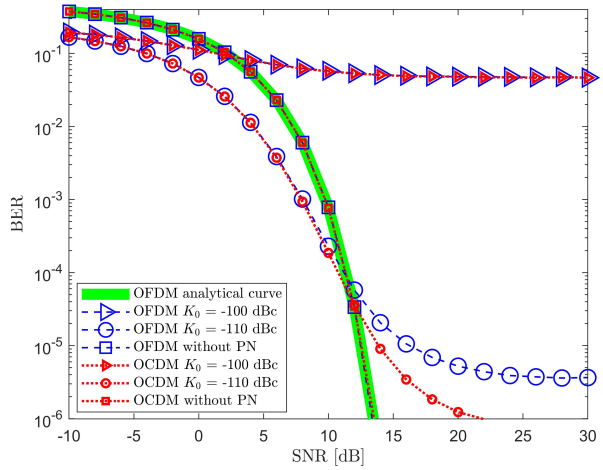

(a) Performance comparison of a 4-QAM OCDM and OFDM system in terms of BER as a function of the SNR for different K_0, and by setting $f_c = 30$ MHz, $B = 5$ GHz, $N = 1024$.

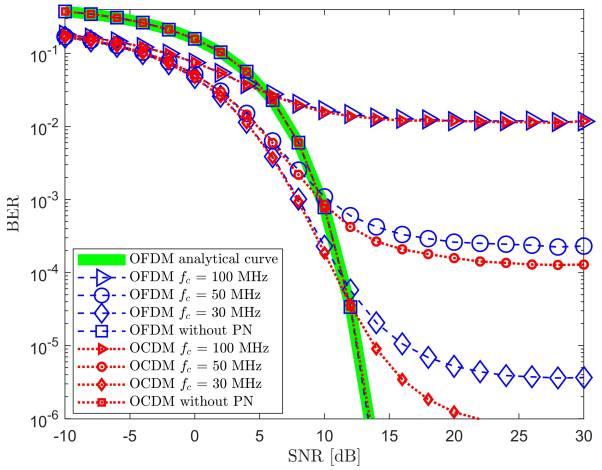

(b) Performance comparison of a 4-QAM OCDM and OFDM system in terms of BER as a function of the SNR for different f_c, and by setting K_0 = -110 dBc/Hz, $B = 5$ GHz, $N = 1024$.

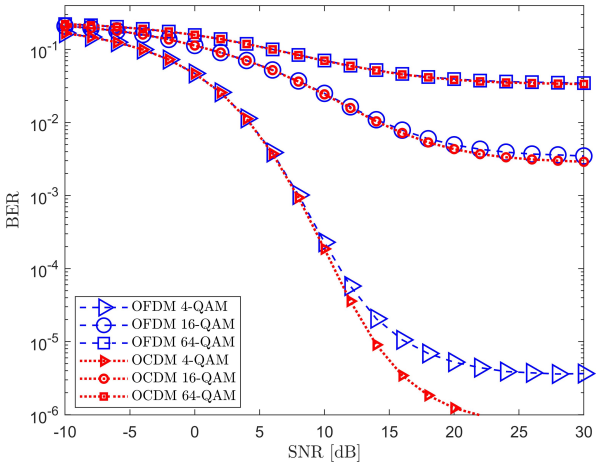

(c) Performance comparison of OCDM and OFDM in terms of BER as a function of the SNR for different modulation orders, and by setting K_0 = -110 dBc/Hz, $f_c = 30$ MHz, $B = 5$ GHz, $N = 1024$.

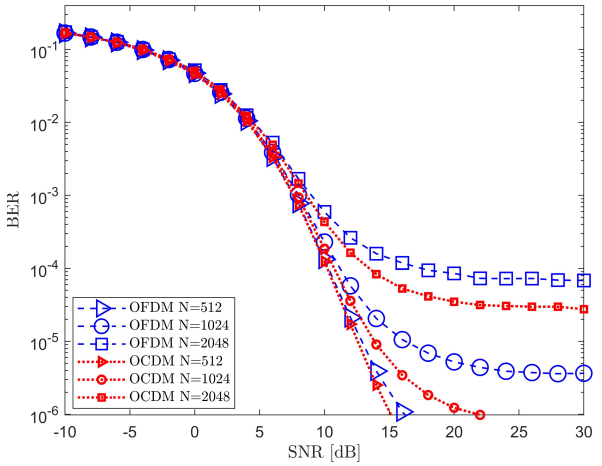

(d) Performance comparison of a 4-QAM OCDM and OFDM systems in terms of BER as a function of the SNR for different N, by setting K_0 = -110 dBc/Hz, $f_c = 30$ MHz, $B = 5$ GHz.

FIGURE 7. BER as a function of the SNR.

Gaussian Noise (AWGN).[7] This alignment serves as a validation of the reliability of our simulator. Additionally, it is worth highlighting that in the low SNR regime (i.e., SNR $<$ 5 dB), the curves corresponding to the cases where the PN is not injected (thus, neither pre-coding nor post-coding is performed) exhibit the worst BER performance; this is an effect of the pre-coding/post-coding performed by the adopted PN compensation algorithm [39], as it doubles the energy per symbol at the expense of halving the symbol rate (the same phenomenon is highlighted in [45, Sec. 4], which is the basis of [39]). Second, as expected, the BER increases with K_0 for the same SNR, which is clearly due to the increased PN power experienced by the receiver. In this regard, it can be seen that, when $K_0 = -100$ dBc/Hz, OCDM and OFDM perform similarly and exhibit an error floor at about $4 \cdot 10^{-2}$. Remarkably, this ceases to be true when (i) $K_0 = -110$ dBc/Hz and (ii) SNR $>$ 10 dB, as OCDM outperforms OFDM, thereby revealing better robustness to CPE and ICI produced by the PN (see Section III-A).

Fig. 7(b) was obtained by considering a 4-QAM modulation and setting $N = 1024$, $B = 5$ GHz, $K_0 = -110$ dBc/Hz, whereas f_c is taken in the set $\{30, 50, 100\}$ MHz. We emphasize again that the choice of K_0 and the interval considered for f_c arise from the characteristics of the reference oscillator. As expected, the BER decreases when the SNR increases, and the performance gets worse for higher values of f_c. Once again, OCDM provides better performance than OFDM when the SNR is sufficiently high, i.e., when the major detrimental effect is caused by the PN.

Fig. 7(c) allows to appreciate the impact on the performance of different modulation orders, namely 4-,

7. In this condition, the well-known mathematical relationship linking BER with SNR for a multi-carrier multiplexing scheme holds [44].

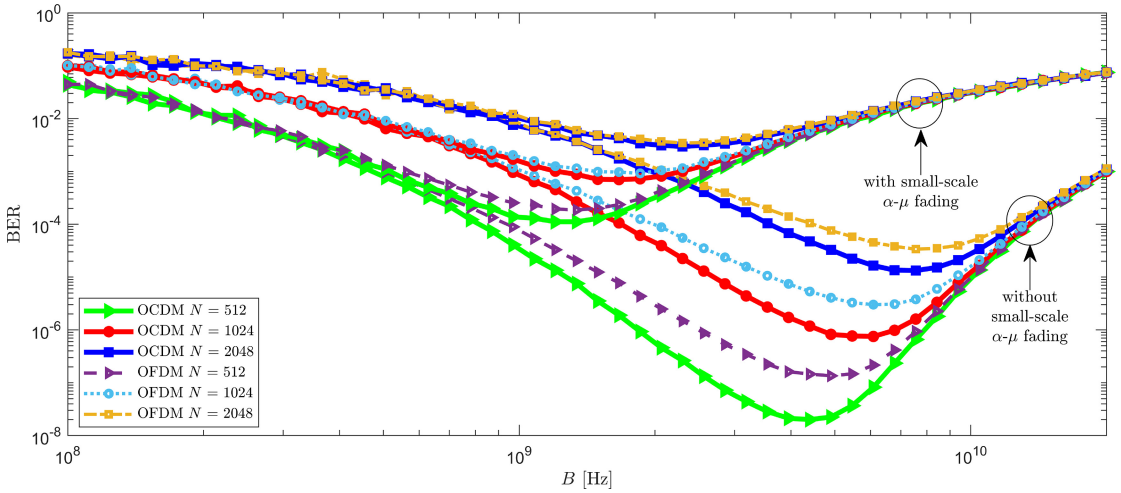

FIGURE 8. Performance comparison of a 4-QAM OCDM and OFDM systems in terms of BER as a function of the bandwidth B, N, and the presence of the small-scale α-μ fading. We set K_0 = -110 dBc/Hz, f_c = 30 MHz, $\alpha = 3.19$, and $\mu = 8.53$.

16-, and 64-QAM. This plot was obtained by setting K_0 = -110 dBc/Hz, f_c = 30 MHz, B = 5 GHz, and $N = 1024$. As can be seen, the BER increases with the modulation order for the same SNR, and the performance gain of OCDM can be better appreciated for lower modulation orders, i.e., when it is easier to counteract the effect of PN.

The purpose of Fig. 7(d) is to assess the impact on performance when varying the number of chirps, N, selected from the set {512, 1024, 2048}. Specifically, the figure was obtained by considering a 4-QAM modulation and by setting K_0 = -110 dBc/Hz, f_c = 30 MHz, and $B = 5$ GHz. It is evident that as the value of N increases while maintaining the same SNR, the BER increases as well. In fact, according to (3), an increase in N while keeping B fixed reduces the distance $\frac{1}{T}$ between the frequency deviations of adjacent chirps (see Fig. 1(a)), thus making the PN impact more detrimental. Furthermore, one can notice that the advantage of OCDM over OFDM becomes more evident as the SNR improves and the value of N decreases.

Finally, Fig. 8 shows the BER as a function of B, also in the presence of the small-scale α-μ fading, by considering 512, 1024, and 2048 chirps, as well as a 4-QAM modulation for both OCDM and OFDM systems. Once again, this plot was obtained by setting $K_0 = -110$ dBc/Hz, and f_c = 30 MHz. It is important to emphasize that each value of B considered in Fig. 8 corresponds to a specific SNR experienced by the receiver, which decreases as the bandwidth increases. Regarding the chosen SNRs values, we set the received power and the additive noise power density to achieve an SNR range from 42 dB (when $B = 100$ MHz) to 19 dB (when $B = 20$ GHz), which is in agreement with the SNRs measured with the 220 GHz test-bed described in [46] that features a SNR of about 35 dB with a bandwidth of 1 GHz (see Table 1 therein). Moreover, as far as the small-scale α-μ fading is concerned, we set $\alpha = 3.19$, and $\mu = 8.53$ to properly reflect the dominance of the direct path in the THz band and by taking inspiration from the study in [36].

Interestingly, all curves show a minimum, which reveals the existence of an optimal value of B that stands out as a trade-off between the frequency separation of adjacent chirps, the PN power, and the SNR. On the one hand, by increasing B for a given value of N, the frequency spacing $\frac{1}{T} = \frac{B}{N}$ between adjacent chirps widens (see Fig. 1(a)), which improves the OCDM immunity to disturbances. On the other hand, increasing B enlarges the power of both the PN and the additive noise, which is instead detrimental to the performance. Hence, the presence of an optimum value of B reveals that the beneficial effect of a wider frequency spacing dominates for sufficiently low values of B, while the negative impact of the other two phenomena (i.e., the increase in the PN power, and the reduction of the SNR) prevails for higher values of B.

In addition, the reader may notice that the optimal value of B increases with N (compare the curves with different markers and refer to the same multiplexing scheme). In fact, when N is higher, the PN is more effective (i.e., the BER is worse), and this implies a right shift of the optimum value of B because the benefit of having widely separated frequency deviations is larger. Besides the obvious increase in the BER, the introduction of the small-scale α-μ fading also results in a reduction of the optimum values of B for each of the investigated schemes (compare the curves with the same markers and refer to the same multiplexing scheme). This is because, in this case, it is preferable to reduce the amount of additive noise introduced in the communication link, rather than counteracting the PN effect by enlarging the frequency spacing between adjacent chirps, i.e., the optimal value of B is lower.

Ultimately, regarding the comparison between OCDM and OFDM, the reader can appreciate that OCDM yields lower BER when B belongs to the interval $[0.4 - 11]$ GHz

and regardless of the presence of the small-scale α-μ fading. Conversely, for the other bandwidth values, the two multiplexing schemes behave similarly. This is because, when $B < 0.4$ GHz, the additive noise effect is negligible and the frequency deviation among adjacent chirps (i.e., $\frac{1}{T} = \frac{B}{N}$) becomes so small that the OCDM resilience to PN cannot be appreciated; on the other hand, when $B > 11$ GHz, the joint effect of additive noise and PN is so high that both techniques provide the same (bad) performance.

V. CONCLUSION

OCDM has recently attracted the attention of the research community as an alternative to OFDM for beyond-5G systems, owing to its increased robustness to severe multipath impairments. As is known, beyond-5G systems are expected to operate also in sub-THz and THz bands, in order to benefit from the availability of larger bandwidths. However, working at such high frequencies poses many challenges, such as the realization of oscillators featuring low PN. Motivated by these considerations, in this paper, we analytically investigated the characteristics of OCDM, and we derived and compared its performance with the well-known OFDM scheme when both are adopted to establish a communication link at 237.7 GHz in the presence of PN.

The signal analysis revealed that the numerical generation of OCDM signals through the IDFnT originates self-chirp interference and inter-chirp interference, which we have shown to be orthogonal to the information-carrying chirps. It turns out, therefore, that these contributions are harmless for the signal that, although significantly impaired, can still be properly demodulated. Contrary to intuition, self- and inter-chirp interference actually provide a benefit by reducing the bandwidth to half when compared to OCDM signals generated based on the continuous-time representation of baseband signals.

Regarding the performance of an OCDM link at 237.7 GHz, we considered the PN characteristics of an actual oscillator, and we implemented a state-of-the-art PN compensation algorithm. The performance comparison with OFDM is proposed as a function of the modulation order, the bandwidth, the number of chirps, and the parameters that define the shape of the PN spectrum. Numerical results show that OCDM outperforms OFDM in high SNR regime and for significant levels of PN. Additionally, our investigation revealed the existence of an optimal value of the bandwidth, which arises as a trade-off between the frequency separation of adjacent chirps, the PN power, and the SNR.

APPENDIX A
PROOF OF (7)

Proof: For the sake of simplicity, we will use the compact notation $\gamma = \frac{B}{T}$ to compute the integral of (7):

$$\begin{aligned}\Psi_k(f) &= \mathcal{F}\left[e^{j\frac{\pi}{4}} e^{-j\pi\gamma\left(t-\frac{k}{B}\right)^2} g_T(t)\right] \\ &= \int_{-\infty}^{\infty} e^{j\frac{\pi}{4}} e^{-j\pi\gamma\left(t-\frac{k}{B}\right)^2} g_T(t) e^{-j2\pi ft} dt \\ &= e^{j\frac{\pi}{4}} \int_0^T e^{-j\pi\gamma\left(t-\frac{k}{B}\right)^2} e^{-j2\pi ft} dt.\end{aligned}$$

By denoting $(t - \frac{k}{B}) = \eta$ it results

$$\begin{aligned}\Psi_k(f) &= e^{j\frac{\pi}{4}} \int_{-\frac{k}{B}}^{T-\frac{k}{B}} e^{-j\pi\gamma\eta^2} e^{-j2\pi f\left(\eta+\frac{k}{B}\right)} d\eta \\ &= e^{j\frac{\pi}{4}} e^{-j2\pi f\frac{k}{B}} \int_{-\frac{k}{B}}^{T-\frac{k}{B}} e^{-j\pi\left[\gamma\eta^2+2f\eta\right]} d\eta \\ &= e^{j\frac{\pi}{4}} e^{-j2\pi f\frac{k}{B}} \int_{-\frac{k}{B}}^{T-\frac{k}{B}} e^{-j\pi\left[\gamma\eta^2+2f\eta+\frac{f^2}{\gamma}\right]} e^{j\pi\frac{f^2}{\gamma}} d\eta\end{aligned}$$

$$\begin{aligned}\Psi_k(f) &= e^{j\frac{\pi}{4}} \frac{e^{j\pi\frac{f^2}{\gamma}} e^{-j2\pi f\frac{k}{B}}}{\sqrt{2\gamma}} \int_{-\sqrt{2\gamma}\frac{k}{B}+\sqrt{\frac{2}{\gamma}}f}^{\sqrt{2\gamma}\left(T-\frac{k}{B}\right)+\sqrt{\frac{2}{\gamma}}f} e^{-j\frac{\pi}{2}\xi^2} d\xi \\ &= e^{j\frac{\pi}{4}} \frac{e^{j\pi\frac{f^2}{\gamma}} e^{-j2\pi f\frac{k}{B}}}{\sqrt{2\gamma}} \left[\int_{-\sqrt{2\gamma}\frac{k}{B}+\sqrt{\frac{2}{\gamma}}f}^{\sqrt{2\gamma}\left(T-\frac{k}{B}\right)+\sqrt{\frac{2}{\gamma}}f} \cos\left(\frac{\pi}{2}\xi^2\right) d\xi - j\int_{-\sqrt{2\gamma}\frac{k}{B}+\sqrt{\frac{2}{\gamma}}f}^{\sqrt{2\gamma}\left(T-\frac{k}{B}\right)+\sqrt{\frac{2}{\gamma}}f} \sin\left(\frac{\pi}{2}\xi^2\right) d\xi\right] \\ &= e^{j\frac{\pi}{4}} \frac{e^{j\pi\frac{f^2}{\gamma}} e^{-j2\pi f\frac{k}{B}}}{\sqrt{2\gamma}} \left[\int_0^{\sqrt{2\gamma}\left(T-\frac{k}{B}\right)+\sqrt{\frac{2}{\gamma}}f} \cos\left(\frac{\pi}{2}\xi^2\right) d\xi - \int_0^{-\sqrt{2\gamma}\frac{k}{B}+\sqrt{\frac{2}{\gamma}}f} \cos\left(\frac{\pi}{2}\xi^2\right) d\xi\right. \\ &\quad \left. - j\int_0^{\sqrt{2\gamma}\left(T-\frac{k}{B}\right)+\sqrt{\frac{2}{\gamma}}f} \sin\left(\frac{\pi}{2}\xi^2\right) d\xi + j\int_0^{-\sqrt{2\gamma}\frac{k}{B}+\sqrt{\frac{2}{\gamma}}f} \sin\left(\frac{\pi}{2}\xi^2\right) d\xi\right] \\ &= e^{j\frac{\pi}{4}} \frac{e^{j\pi\frac{f^2}{\gamma}} e^{-j2\pi f\frac{k}{B}}}{\sqrt{2\gamma}} \left[\mathrm{C}\left(\sqrt{2\gamma}\left(T-\frac{k}{B}\right)+\sqrt{\frac{2}{\gamma}}f\right) - \mathrm{C}\left(-\sqrt{2\gamma}\frac{k}{B}+\sqrt{\frac{2}{\gamma}}f\right)\right. \\ &\quad \left. - j\mathrm{S}\left(\sqrt{2\gamma}\left(T-\frac{k}{B}\right)+\sqrt{\frac{2}{\gamma}}f\right) + j\mathrm{S}\left(-\sqrt{2\gamma}\frac{k}{B}+\sqrt{\frac{2}{\gamma}}f\right)\right] \qquad (24)\end{aligned}$$

$$= e^{j\frac{\pi}{4}} e^{j\pi\frac{f^2}{\gamma}} e^{-j2\pi f\frac{k}{B}} \int_{-\frac{k}{B}}^{T-\frac{k}{B}} e^{-j\pi\left[\sqrt{\gamma}\eta+\frac{f}{\sqrt{\gamma}}\right]^2} d\eta.$$

By letting $\sqrt{\gamma}\eta + \frac{f}{\sqrt{\gamma}} = \frac{\xi}{\sqrt{2}}$ we obtain $\Psi_k(f)$ as in (24), shown at the bottom of the previous page, where $C(z) \triangleq \int_0^z \cos\left(\frac{\pi t^2}{2}\right) dt$ is the Fresnel cosine integral function and $S(z) \triangleq \int_0^z \sin\left(\frac{\pi t^2}{2}\right) dt$ is the Fresnel sine integral function. ■

APPENDIX B
PROOF OF (14)

Proof: By letting $\theta_k^{(m)}(t) = \frac{\pi}{4} - \pi\frac{B}{T}(t - \frac{k}{B} + mT)^2$ in (14), so that we can write $\psi_k^{(m)}(t) = e^{j\theta_k^{(m)}(t)}$, it follows that the instantaneous frequency deviation of $\psi_k^{(m)}(t)$ is

$$\begin{aligned}\Delta f_k^{(m)}(t) &= \frac{1}{2\pi}\frac{d\theta_k^{(m)}(t)}{dt} \\ &= \frac{k}{T} - \frac{B}{T}t - mB,\end{aligned}$$

which, compared with (6), shows that the frequency sweep interval of $\psi_k^{(m)}(t)$ is translated of mB with respect to the sweep interval of $\psi_k(t)$, thus corresponding to the mth spectrum repetition. ■

APPENDIX C
PROOF OF (16)

Proof: Given (4) and (14) $\langle\psi_k(t), \psi_i^{(m)}(t)\rangle$ can be computed as (25), shown at the bottom of the page. One observes that $\forall i \in \mathbb{Z}$ and $\forall m \in \mathbb{Z}$ it is $e^{j2\pi mi} = 1$. This results in (26), shown at the bottom of the page. ■

APPENDIX D
THERMAL NOISE

Wireless communications are known to be affected by the presence of thermal noise, which deserves a specific discussion when it comes to the THz band. As is well known, this type of noise, which has Gaussian statistics, is added to the useful signal at various points between the source and destination, including the receiving circuits. However, for the purposes of analysis, it is usually lumped into one source, added to the information-bearing signal at the input of the receiver, whose two-sided PSD is [35]:

$$\begin{aligned}\langle\psi_k(t), \psi_i^{(m)}(t)\rangle &= \int_0^T \psi_k(t)\left[\psi_i^{(m)}(t)\right]^* dt \\ &= \int_0^T e^{j\frac{\pi}{4}} e^{-j\pi\frac{B}{T}\left(t-\frac{k}{B}\right)^2} e^{-j\frac{\pi}{4}} e^{j\pi\frac{B}{T}\left(t-\frac{i}{B}+mT\right)^2} dt \\ &= \int_0^T e^{-j\pi\frac{B}{T}\left(t-\frac{k}{B}\right)^2} e^{j\pi\frac{B}{T}\left(t-\frac{i}{B}+mT\right)^2} dt \\ &= \int_0^T e^{-j\pi\frac{B}{T}\left(t^2+\frac{k^2}{B^2}-2\frac{k}{B}t\right)} e^{j\pi\frac{B}{T}\left(t^2+\frac{i^2}{B^2}+m^2T^2-2\frac{i}{B}t+2mTt-2\frac{mi}{B}T\right)} dt \\ &= \int_0^T e^{-j\pi\frac{k^2}{BT}} e^{j2\pi\frac{k}{T}t} e^{j\pi\frac{i^2}{BT}} e^{j\pi m^2BT} e^{-j2\pi\frac{i}{T}t} e^{j2\pi mBt} e^{-j2\pi mi} dt \\ &= e^{j\pi\frac{(i^2-k^2)}{N}} e^{j\pi Nm^2} e^{-j2\pi mi} \int_0^T e^{j\frac{2\pi}{T}(k-i)t} e^{j2\pi mBt} dt. \end{aligned} \tag{25}$$

$$\begin{aligned}\langle\psi_k(t), \psi_i^{(m)}(t)\rangle &= e^{j\pi\frac{(i^2-k^2)}{N}} e^{j\pi Nm^2} \int_0^T e^{j\frac{2\pi}{T}(k-i)t} e^{j2\pi mBt} dt \\ &= e^{j\pi\frac{(i^2-k^2)}{N}} e^{j\pi Nm^2} \int_0^T e^{j\frac{2\pi}{T}(k-i)t} e^{j\frac{2\pi}{T}mNt} dt \\ &= e^{j\pi\frac{(i^2-k^2)}{N}} e^{j\pi Nm^2} \int_0^T e^{j\frac{2\pi}{T}(k-i+mN)t} dt \\ &= e^{j\pi\frac{(i^2-k^2)}{N}} e^{j\pi Nm^2} \frac{e^{j2\pi(k-i+mN)} - 1}{j\frac{2\pi}{T}(k-i+mN)} \\ &= -jTe^{j\pi\frac{(i^2-k^2)}{N}} e^{j\pi Nm^2} \frac{e^{j2\pi(k-i+mN)} - 1}{2\pi(k-i+mN)} \\ &= -jTe^{j\pi\frac{(i^2-k^2)}{N}} e^{j\pi Nm^2} e^{j\pi(k-i+mN)} \frac{e^{j\pi(k-i+mN)} - e^{-j\pi(k-i+mN)}}{2\pi(k-i+mN)} \\ &= -jTe^{j\pi\frac{(i^2-k^2)}{N}} e^{j\pi Nm^2} e^{j\pi(k-i+mN)} \frac{j2\sin(\pi(k-i+mN))}{2\pi(k-i+mN)} \\ &= T\text{sinc}\Big(k-i+mN\Big) e^{j\pi\frac{(i^2-k^2)}{N}} e^{j\pi Nm^2} e^{j\pi(k-i+mN)}. \end{aligned} \tag{26}$$

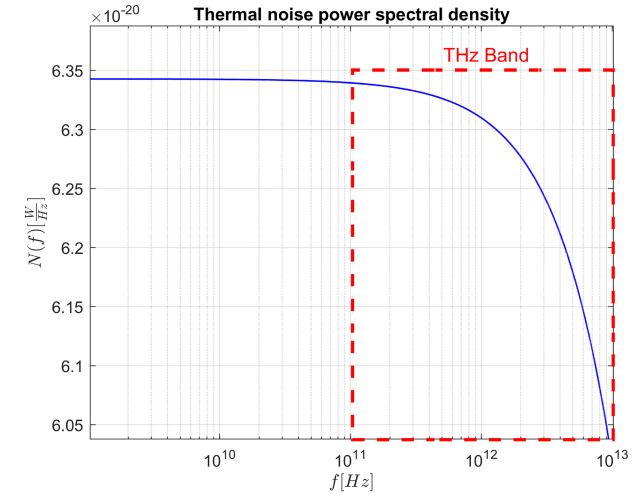

(a) Thermal noise PSD for positive frequencies up to 10 THz.

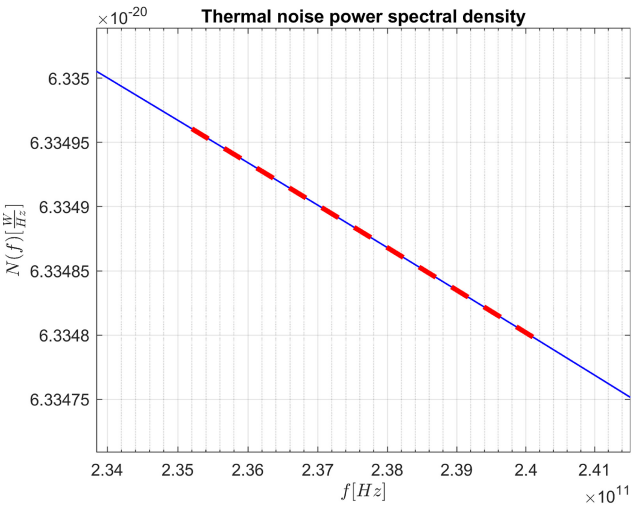

(b) Thermal noise PSD in a bandwidth $B = 5$ GHz centered at $f_0 = 237.7$ GHz.

FIGURE 9. Thermal noise PSD.

$$N(f) = \frac{h_p|f|}{2\left(e^{\frac{h_p|f|}{kT_{sys}}} - 1\right)} \quad \left[\frac{W}{Hz}\right], \tag{27}$$

where h_p is the Planck's constant, k is the Boltzmann's constant, and T_{sys} is the system noise temperature. When $\frac{h_p|f|}{kT_{sys}} \ll 1$, that is for $|f| \ll \frac{kT_{sys}}{h_p}$, an approximated, simpler, expression of (27) is obtained, which is usually denoted as N_0:

$$N_0 \simeq \frac{1}{2}kT_{sys} \quad \left[\frac{W}{Hz}\right]. \tag{28}$$

Since the right-hand side of (28) does not depend on f, and given the Gaussian and additive nature of the thermal noise, it is customary to denote it as AWGN. However, for reasonable values of T_{sys}, the condition $|f| \ll \frac{kT_{sys}}{h_p}$ is not fulfilled in the THz band, which makes (27) the only accurate expression for the thermal noise PSD in this frequency range. This is clearly evident in Fig. 9(a), which shows $N(f)$ for positive frequencies when the receiver noise figure F is equal to 12 dB.[8] This is the reason why, throughout the paper, we have generically used the term "thermal noise" instead of the more common acronym "AWGN".

Nevertheless, when it comes to practical systems operating with a carrier frequency f_0 in the THz band, assuming a constant PSD $N(f) \simeq N(f_0)$ might still be reasonable, provided that (27) does not change significantly within the signal bandwidth. Fig. 9(b) gives a quantitative measure about the error introduced assuming $N(f) \simeq N(f_0)$ when $F = 12$ dB and considering a bandwidth B of 5 GHz centered around the carrier $f_0 = 237.7$ GHz considered in this paper.[9] Focusing the attention on the dashed red line, it clearly appears that $\max_{f\in B} \frac{|N(f)-N(f_0)|}{N(f_0)} \cdot 100 = 0.0013\%$, which confirms that such variations can be neglected. In light of the above, our numerical results were obtained by considering a flat spectrum for the Gaussian thermal noise.

APPENDIX E
MOLECULAR NOISE

The molecular noise, as the name suggests, originates from interactions of electromagnetic waves with the molecules of the medium in which it is propagating. More precisely, the wave energy is partially absorbed by the molecules and re-emitted into the channel, which causes a disturbance. The intensity of this phenomenon depends on the frequency, which results in a colored spectrum with peaks at specific frequencies (resonance frequencies). Since the number of molecules, along with the number of resonances per molecule, satisfies the assumptions of the central limit theorem, it has a Gaussian statistic.

Coming to the two-sided PSD of the molecular noise, its expression is as shown in equation (29), shown at the bottom of the page [51] where d is the Tx-Rx distance, h_p and k are the Planck's and Boltzmann's constants, respectively, c is the speed of light in vacuum, T_0 is the reference temperature of the atmosphere, n_c is the index of refraction which refers to the carrier frequency f_0, $S(f)$ is the one-sided PSD of the THz signal, n is the index of refraction seen by the THz wave, and $k(f)$ is the medium absorption coefficient,

8. This value of receiver noise figure belongs to the range of 10-15 dB that is provided by current integrated circuit technologies at THz frequencies [47], [48], [49], [50].

9. This carrier frequency is the one used by the reference oscillator in [33], whereas the bandwidth value is compatible with the IEEE 802.15.3d standard [34], since the latter considers nearby carrier frequencies.

$$N_m(d,f) = \frac{h_p\pi|f|^3}{c^2}\left(e^{\frac{h_p|f|}{kT_0}} - 1\right)^{-1}\left(\frac{c}{\sqrt{4\pi}n_c f_0}\right)^2 + \frac{S(|f|)}{2}\left(1 - e^{-k(|f|)d}\right)\left(\frac{c}{4\pi ndf}\right)^2\left[\frac{W}{Hz}\right], \tag{29}$$

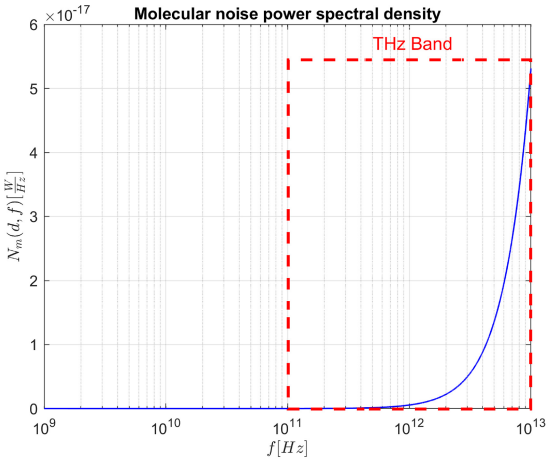

(a) Molecular noise PSD for positive frequencies up to 10 THz.

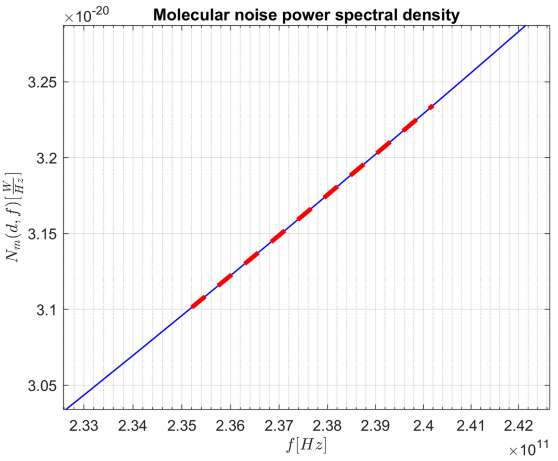

(b) Molecular noise PSD in a bandwidth $B = 5$ GHz centered at $f_0 = 237.7$ GHz.

FIGURE 10. Molecular noise PSD.

that is, the parameter describing the medium absorption area of the molecules per unit volume. In fact, the exponential term $e^{-k(f)d}$ represents the molecular absorption gain, as a function of $k(f)$ and d.

Fig. 10(a) shows an example of $N_m(d,f)$ for positive frequencies up to 10 THz. The parameter settings used for this plot are reported in Table 1, where:

- The value of the carrier frequency, f_0, is the one used by our reference oscillator [33];
- The value of the carrier frequency, f_0, and bandwidth, B, is consistent with the carrier frequencies and bandwidths considered by the IEEE 802.15.3d standard [34];
- An array of CMOS-based THz sources, which exploits several frequency multipliers to generate a THz carrier, can radiate approximately -10 dBm at 0.4 THz, so we have been conservative in considering $P_T = -10$ dBm at 0.2377 THz [52], [53];
- The value of $k(f_0)$ is the average of the molecular absorption coefficients that characterize a $B = 5$ GHz bandwidth centered around a $f_0 = 237.7$ GHz carrier. Such coefficients have been taken from the TeraSim simulator [54].

TABLE 1. Parameter settings for Fig. 10.

Parameter	Value
f_0	237.7 GHz
B	5 GHz
d	1 m
T_0	290 K
P_T	-10 dBm
$k(f_0)$	$\simeq 5.91 \cdot 10^{-4}\ m^{-1}$
n, n_c	1

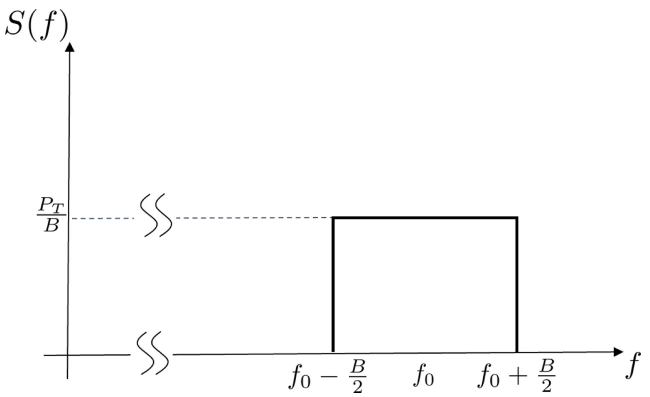

FIGURE 11. Signal spectrum assumed to derive $N_m(d, f)$.

Again, in Fig. 10(a), the THz band has been highlighted with a dashed red box. It can be immediately observed that, in contrast to the thermal noise spectrum, $N_m(d,f)$ increases in the THz band. For the sake of completeness, we remark that $N_m(d,f)$ goes to 0 for $f >> 10^{13}$, that is, outside the THz band.

It is worth noting that the shape of $N_m(d,f)$ depends on $S(f)$, which is the one-sided PSD of the transmitted signal. To obtain Fig. 10(a), the latter was assumed to have a rectangular shape, as depicted in Fig. 11. Moreover, without loss of generality, we considered a constant value of $k(f_0)$ over B.

All that said, let us focus our attention on the shape of the spectrum within the band of interest for this paper. In this regard, Fig. 10(b) is a zoomed-in version of Fig. 10(a), highlighting the molecular noise spectrum in the considered band B of 5 GHz centered at $f_0 = 237.7$ GHz. It turns out that, within B, it is $\max_{f \in B} \frac{|N_m(f) - N_m(f_0)|}{N_m(f_0)} \cdot 100 \approx 2.1\%$. Given the small deviation of the spectrum in the considered band, in this paper we considered that taking $N_m(f) = N_m(f_0)$ within the bandwidth B of interest was a reasonable assumption. Similarly to the case of the thermal noise, therefore, our numerical results have been obtained assuming a flat spectrum for the Gaussian molecular noise within the bandwidth of interest.

REFERENCES

[1] W. Jiang, B. Han, M. A. Habibi, and H. D. Schotten, "The road towards 6G: A comprehensive survey," *IEEE Open J. Communi. Soc.*, vol. 2, pp. 334–366, 2021.

[2] X. Ouyang and J. Zhao, "Orthogonal chirp division multiplexing," *IEEE Trans. Commun.*, vol. 64, no. 9, pp. 3946–3957, Sep. 2016.

[3] X. Ouyang, O. A. Dobre, Y. L. Guan, and J. Zhao, "Chirp spread spectrum toward the Nyquist signaling rate—Orthogonality condition and applications," *IEEE Signal Process. Lett.*, vol. 24, no. 10, pp. 1488–1492, Oct. 2017.

[4] A. Bemani, G. Cuozzo, N. Ksairi, and M. Kountouris, "Affine frequency division multiplexing for next-generation wireless networks," in *Proc. 17th Int. Symp. Wireless Commun. Syst. (ISWCS)*, 2021, pp. 1–6.

[5] M. S. Omar and X. Ma, "Performance analysis of OCDM for wireless communications," *IEEE Trans. Wireless Commun.*, vol. 20, no. 7, pp. 4032–4043, Jul. 2021.

[6] X. Ouyang, C. Antony, G. Talli, and P. D. Townsend, "Robust channel estimation for coherent optical orthogonal chirp-division multiplexing with pulse compression and noise rejection," *J. Lightwave Technol.*, vol. 36, no. 23, pp. 5600–5610, Dec. 2018.

[7] L. G. d. Oliveira, M. B. Alabd, B. Nuss, and T. Zwick, "An OCDM radar-communication system," in *Proc. 14th Eur. Conf. Antennas Propag. (EuCAP)*, 2020, pp. 1–5.

[8] L. G. De Oliveira, B. Nuss, M. B. Alabd, Y. Li, L. Yu, and T. Zwick, "MIMO-OCDM-based joint radar sensing and communication," in *Proc. 15th Eur. Conf. Antennas Propag. (EuCAP)*, 2021, pp. 1–5.

[9] L. Giroto de Oliveira et al., "Discrete-fresnel domain channel estimation in OCDM-based radar systems," *IEEE Trans. Microw. Theory Techn.*, vol. 71, no. 5, pp. 2258–2275, May 2023.

[10] S.-H. Wang, C.-P. Li, K.-C. Lee, and H.-J. Su, "A novel low-complexity precoded OFDM system with reduced PAPR," *IEEE Trans. Signal Process.*, vol. 63, no. 6, pp. 1366–1376, Mar. 2015.

[11] M. Polese, J. M. Jornet, T. Melodia, and M. Zorzi, "Toward end-to-end, full-stack 6G terahertz networks," *IEEE Commun. Mag.*, vol. 58, no. 11, pp. 48–54, Nov. 2020.

[12] C. Chaccour, M. N. Soorki, W. Saad, M. Bennis, P. Popovski, and M. Debbah, "Seven defining features of terahertz (THz) wireless systems: A fellowship of communication and sensing," 2021, *arXiv:2102.07668*.

[13] I. F. Akyildiz, J. M. Jornet, and C. Han, "Terahertz band: Next frontier for wireless communications," *Phys. Commun.*, vol. 12, pp. 16–32, Sep. 2014.

[14] N. Rajatheva et al., "Scoring the terabit/s goal: Broadband connectivity in 6G," 2021, *arXiv:2008.07220*.

[15] I. F. Akyildiz, J. M. Jornet, and C. Han, "TeraNets: Ultra-broadband communication networks in the terahertz band," *IEEE Wireless Commun.*, vol. 21, no. 4, pp. 130–135, Aug. 2014.

[16] Z. Chen et al., "Terahertz wireless communications for 2030 and beyond: A cutting-edge frontier," *IEEE Commun. Mag.*, vol. 59, no. 11, pp. 66–72, Nov. 2021.

[17] T. S. Rappaport et al., "Wireless communications and applications above 100 GHz: Opportunities and challenges for 6G and beyond," *IEEE Access*, vol. 7, pp. 78729–78757, 2019.

[18] C. Barrett, *Fractional/Integer-N PLL Basics*, Texas Instrum. Semicond. Manuf. Co., Dallas, TX, USA, 1999.

[19] Y. Bai and P.-J. Bouvet, "Orthogonal chirp division multiplexing for underwater acoustic communication," *Sensors*, vol. 18, no. 11, p. 3815, 2018.

[20] P. Zhu, X. Xu, X. Tu, Y. Chen, and Y. Tao, "Anti-multipath orthogonal chirp division multiplexing for underwater acoustic communication," *IEEE Access*, vol. 8, pp. 13305–13314, 2020.

[21] R. Bomfin, M. Chafii, and G. Fettweis, "Performance assessment of orthogonal chirp division multiplexing in MIMO space time coding," in *Proc. IEEE 2nd 5G World Forum (5GWF)*, 2019, pp. 220–225.

[22] Y. Yin, "The CPDA detector for the MIMO OCDM system," in *Proc. IEEE 6th Int. Conf. Comput. Commun. Syst. (ICCCS)*, 2021, pp. 1001–1004.

[23] L. de M. B. A. Dib, G. R. Colen, M. De L. Filomeno, and M. V. Ribeiro, "Orthogonal chirp division multiplexing for baseband data communication systems," *IEEE Syst. J.*, vol. 14, no. 2, pp. 2164–2174, Jun. 2020.

[24] L. Giroto de Oliveira, M. De Lima Filomeno, H. V. Poor, and M. Vidal Ribeiro, "Orthogonal chirp-division multiplexing for power line sensing via time-domain reflectometry," *IEEE Sensors J.*, vol. 21, no. 2, pp. 955–964, Jan. 2021.

[25] M. S. Omar and X. Ma, "Designing OCDM-based multi-user transmissions," in *Proc. IEEE Global Commun. Conf. (GLOBECOM)*, 2019, pp. 1–6.

[26] C. Buratti, G. Cuozzo, and R. Verdone, "OCDMA: A MAC protocol for industrial intra-machine terahertz network," *J. Infrared, Millim. Thz. Waves*, vol. 43, pp. 400–425, Apr. 2022.

[27] R. Bomfin, M. Chafii, and G. Fettweis, "Low-complexity iterative receiver for orthogonal chirp division multiplexing," in *Proc. IEEE Wireless Commun. Netw. Conf. Workshop (WCNCW)*, 2019, pp. 1–6.

[28] R. Bomfin, M. Chafii, and G. Fettweis, "A novel iterative receiver design for CP-free transmission under frequency-selective channels," *IEEE Commun. Lett.*, vol. 24, no. 3, pp. 525–529, Mar. 2020.

[29] X. Wang, Z. Jiang, and X.-H. Shen, "Low complexity equalization of orthogonal chirp division multiplexing in doubly-selective channels," *Sensors*, vol. 20, no. 11, p. 3125, 2020.

[30] X. Wang, X. Shen, F. Hua, and Z. Jiang, "On low-complexity MMSE channel estimation for OCDM systems," *IEEE Wireless Commun. Lett.*, vol. 10, no. 8, pp. 1697–1701, Aug. 2021.

[31] A. A. A. Solyman et al., "A low-complexity equalizer for video broadcasting in cyber-physical social systems through Handheld mobile devices," *IEEE Access*, vol. 8, pp. 67591–67602, 2020.

[32] M. S. Omar and X. Ma, "Spectrum design for orthogonal chirp division multiplexing transmissions," *IEEE Wireless Commun. Lett.*, vol. 9, no. 11, pp. 1990–1994, Nov. 2020.

[33] X. Liu and H. C. Luong, "A fully integrated 0.27-THz injection-locked frequency synthesizer with frequency-tracking loop in 65-nm CMOS," *IEEE J. Solid-State Circuits*, vol. 55, no. 4, pp. 1051–1063, Apr. 2020.

[34] "IEEE standard for high data rate wireless multi-media networks–Amendment 2: 100 Gb/s wireless switched point-to-point physical layer," IEEE Standard 802.15.3d-2017, *(Amendment IEEE Standard 802.15.3-2016 and IEEE Standard 802.15.3e-2017)*, 2017.

[35] A. B. Carlson and P. B. Crilly, *Communication Systems: An Introduction to Signals and Noise in Electrical Communication*, McGraw-Hill Publ. co., New York, NY, USA: 2010.

[36] E. N. Papasotiriou, A.-A. A. Boulogeorgos, K. Haneda, M. F. de Guzman, and A. Alexiou, "An experimentally validated fading model for THz wireless systems," *Sci. Rep.*, vol. 11, no. 1, 2021, Art. no. 18717.

[37] S. Bicais and J.-B. Dore, "Phase noise model selection for sub-THz communications," in *Proc. IEEE Global Commun. Conf. (GLOBECOM)*, 2019, pp. 1–6.

[38] E. N. Papasotiriou, A.-A. A. Boulogeorgos, and A. Alexiou, "Fading modeling in indoor thz wireless systems," in *Proc. Int. Balkan Conf. Commun. Netw. (BalkanCom)*, 2021, pp. 161–165.

[39] H.-G. Ryu, Y. Li, and J.-S. Park, "An improved ICI reduction method in OFDM communication system," *IEEE Trans. Broadcast.*, vol. 51, no. 3, pp. 395–400, Sep. 2005.

[40] M. Seo, M. Urteaga, M. Rodwell, and M. Choe, "A 300 GHz PLL in an InP HBT technology," in *Proc. IEEE MTT-S Int. Microw. Symp.*, 2011, p. 1.

[41] Z. Chen et al., "A U-band PLL using implicit distributed resonators for sub-THz wireless transceivers in 40 nm CMOS," *IEEE Trans. Circuits Syst. II, Exp. Briefs*, vol. 67, no. 9, pp. 1574–1578, Sep. 2020.

[42] A. Demir, "Computing timing jitter from phase noise spectra for oscillators and phase-locked loops with white and $1/f$ noise," *IEEE Trans. Circuits Syst. I, Reg. Papers*, vol. 53, no. 9, pp. 1869–1884, Sep. 2006.

[43] H. Mehrpouyan, M. R. Khanzadi, M. Matthaiou, A. M. Sayeed, R. Schober, and Y. Hua, "Improving bandwidth efficiency in E-band communication systems," *IEEE Commun. Mag.*, vol. 52, no. 3, pp. 121–128, Mar. 2014.

[44] A. B. Narasimhamurthy, M. K. Banavar, and C. Tepedelenlioğlu, *OFDM Systems for Wireless Communications*. Cham, Switzerland, Springer, 2010, pp. 1–3.

[45] Y. Zhao and S.-G. Haggman, "Intercarrier interference self-cancellation scheme for OFDM mobile communication systems," *IEEE Trans. Commun.*, vol. 49, no. 7, pp. 1185–1191, Jul. 2001.

[46] P. Sen, V. Ariyarathna, A. Madanayake, and J. M. Jornet, "Experimental wireless testbed for ultrabroadband terahertz networks," in *Proc. 14th Int. Workshop Wireless Netw. Testbeds, Exp. Eval. Charact.*, 2020, pp. 48–55.
[47] I. Kallfass et al., "64 Gbit/s transmission over 850 m fixed wireless link at 240 GHz carrier frequency," *J. Infrared, Millim. Thz Waves*, vol. 36, no. 2, pp. 221–233, 2015.
[48] K. Rikkinen, P. Kyosti, M. E. Leinonen, M. Berg, and A. Parssinen, "THz radio communication: Link budget analysis toward 6G," *IEEE Commun. Mag.*, vol. 58, no. 11, pp. 22–27, Nov. 2020.
[49] P. Rodríguez-Vázquez, M. E. Leinonen, J. Grzyb, N. Tervo, A. Parssinen, and U. R. Pfeiffer, "Signal-processing challenges in leveraging 100 Gb/s wireless THz," in *Proc. 2nd 6G Wireless Summit (6G SUMMIT)*, 2020, pp. 1–5.
[50] T. Schneider, A. Wiatrek, S. Preussler, M. Grigat, and R.-P. Braun, "Link budget analysis for terahertz fixed wireless links," *IEEE Trans. Thz. Sci. Technol.*, vol. 2, no. 2, pp. 250–256, Mar. 2012.
[51] R. Zhang, K. Yang, Q. H. Abbasi, K. A. Qaraqe, and A. Alomainy, "Analytical modelling of the effect of noise on the terahertz in-vivo communication channel for body-centric nano-networks," *Nano Commun. Netw.*, vol. 15, pp. 59–68, Mar. 2018.
[52] U. R. Pfeiffer, R. Jain, J. Grzyb, S. Malz, P. Hillger, and P. Rodríguez-Vízquez, "Current status of terahertz integrated circuits-from components to systems," in *Proc. IEEE BiCMOS Compound Semicond. Integr. Circuits Technol. Symp. (BCICTS)*, 2018, pp. 1–7.
[53] R. Han et al., "Filling the gap: Silicon terahertz integrated circuits offer our best bet," *IEEE Microw. Mag.*, vol. 20, no. 4, pp. 80–93, Apr. 2019.
[54] Z. Hossain, Q. Xia, and J. M. Jornet, "TeraSim: An ns-3 extension to simulate terahertz-band communication networks," *Nano Commun. Netw.*, vol. 17, pp. 36–44, Sep. 2018.

GIAMPAOLO CUOZZO (Member, IEEE) was born in Salerno, Italy, in 1995. He received the B.Sc. degree (with Hons.) in electronics and telecommunications engineering, the M.Sc. degree (with Hons.) in telecommunications engineering, and the Ph.D. degree in electronics, telecommunications, and information technologies engineering from the University of Bologna in 2017, 2019, and 2022, respectively.

He is currently the Head of Research with the National Laboratory of Wireless Communications, CNIT (the National, Inter-University Consortium for Telecommunications). He is the author of one book, one invention, and ten articles. His research activity is focused on the study, development, and validation of wireless networks for the Industrial Internet of Things, with a particular focus on signal processing techniques and MAC protocol design for THz-based systems, as well as scheduling optimization algorithms for 5G NR networks. His interests also include experimental activities that exploit current wireless technologies, like 5G, LoRa, ZigBee, and NB-IoT.

NICOLÒ LONGHI (Graduate Student Member, IEEE) was born in Ostiglia, Italy, in 1997. He received the B.Sc. degree in electronics and telecommunications engineering and the M.Sc. degree (with Hons.) in telecommunications engineering from the University of Bologna, Italy, in 2019 and 2021, respectively, where he is currently pursuing the Ph.D. degree in electronics, telecommunications, and information technologies engineering, funded by Telecom Italia S.p.A.

He is a Research Associate with the National Laboratory of Wireless Communications, CNIT (the National, Inter-University Consortium for Telecommunications). His research activity is on 5G and 6G cellular networks for Industrial Internet of Things applications, with a particular focus on scheduling, signal processing, and O-RAN systems. His interests lie in the study, development, and implementation of wireless IoT and IIoT testbeds.

GIANNI PASOLINI (Member, IEEE) received the M.Sc. degree in telecommunications engineering and the Ph.D. degree in electronic engineering and computer science from the University of Bologna, Italy, in 1999 and 2003, respectively. He is currently an Associate Professor with the Department of Electrical, Electronic and Information Engineering, University of Bologna, where he has been teaching various courses in the field of telecommunications since 2003. His major field of study includes wireless communication systems, Internet of Things, digital signal processing, and THz communications. Throughout his career, he has actively participated in several European initiatives focused on wireless communications, including COST actions and networks of excellence. He was the recipient of the Best Paper Award at the 2023 IEEE International Conference on Communications. He is one of the founding members of the National Laboratory of Wireless Communications—WiLab of the National Inter-University Consortium for Telecommunications (CNIT) in Italy. He serves as an Associate Editor for the IEEE OPEN JOURNAL OF THE COMMUNICATIONS SOCIETY. He also served as a member of the Organizing Committee for the 2018 IEEE International Symposium on Personal, Indoor and Mobile Radio Communications, the 2017 IEEE International Symposium on Wireless Communication Systems, and the 2011 IEEE International Conference on Ultra-Wideband.